AGU PUBLICATIONS

JGR

Journal of Geophysical Research: Atmospheres

RESEARCH ARTICLE
10.1002/2015JD023634

Key Points:
- Aircraft sampled microphysical and aerosol fields are used to evaluate WRF-Chem
- Westward propagation of the monsoon depression reduced AOD over central India
- Aerosol-induced perturbations invigorated convection via low-level heating and cloud physics

Correspondence to:
S. N. Tripathi,
snt@iitk.ac.in

Citation:
Sarangi, C., S. N. Tripathi, S. Tripathi, and M. C. Barth (2015), Aerosol-cloud associations over Gangetic Basin during a typical monsoon depression event using WRF-Chem simulation, *J. Geophys. Res. Atmos.*, *120*, 10,974–10,995 doi:10.1002/2015JD023634.

Received 7 MAY 2015
Accepted 15 SEP 2015
Accepted article online 19 SEP 2015
Published online 30 OCT 2015

©2015. American Geophysical Union. All Rights Reserved.

Aerosol-cloud associations over Gangetic Basin during a typical monsoon depression event using WRF-Chem simulation

Chandan Sarangi[1], S. N. Tripathi[1], Shivam Tripathi[1], and Mary C. Barth[2]

[1]Department of Civil Engineering, Indian Institute of Technology, Kanpur, India, [2]Atmospheric Chemistry Observations and Modeling Laboratory, NCAR, Boulder, Colorado, USA

Abstract To study aerosol-cloud interactions over the Gangetic Basin of India, the Weather Research and Forecasting model coupled with chemistry (WRF-Chem) has been applied to a typical monsoon depression event prevalent between the 23 and 29 August 2009. This event was sampled during the Cloud Aerosol Interaction and Precipitation Enhancement EXperiment (CAIPEEX) aircraft campaign, providing measurements of aerosol and cloud microphysical properties from two sorties. Comparison of the simulated meteorological, thermodynamical, and aerosol fields against satellite and in situ aircraft measurements illustrated that the westward propagation of the monsoon depression and the cloud, aerosol, and rainfall spatial distribution was simulated reasonably well using anthropogenic emission rates from Monitoring Atmospheric Composition and Climate project along with cityZEN projects (MACCity)+Intercontinental Chemical Transport Experiment Phase B anthropogenic emission rates. However,the magnitude of aerosol optical depth was underestimated by up to 50%. A simulation with aerosol emissions increased by a factor of 6 over the CAIPEEX campaign domain increased the simulated aerosol concentrations to values close to the observations, mainly within boundary layer. Comparison of the low-aerosol simulation and high-aerosol simulation for the two sorties illustrated that more anthropogenic aerosols increased the cloud condensing nuclei (CCN) and cloud droplet mass concentrations. The number of simulated cloud droplets increased while the cloud droplet effective radii decreased, highlighting the importance of CCN-cloud feedbacks over this region. The increase in simulated anthropogenic aerosols (including absorbing aerosols) also increased the temperature of air parcels below clouds and thus the convective available potential energy (CAPE). The increase in CAPE intensified the updraft and invigorated the cloud, inducing formation of deeper clouds with more ice-phase hydrometeors for both cases. These case studies provide evidence of aerosol-induced cloud invigoration over the Gangetic Basin.

1. Introduction

Anthropogenic aerosols play a fundamental role in cloud formation by serving as cloud condensation nuclei (CCN). An increase in CCN number is associated with an increase in cloud droplet number but a decrease in droplet effective size, and thereby causing an enhancement in cloud albedo [*Twomey*, 1977] and cloud lifetime [*Albrecht*, 1989]. This aerosol-induced decrease in droplet size is suggested to reduce the collision and coalescence efficiency and thereby suppressing surface precipitation, mostly in warm clouds [*Givati and Rosenfeld*, 2004; *Tao et al.*, 2007]. Although these aerosol-induced perturbations in warm clouds are fairly well understood and documented in recent studies [*Intergovernmental Panel on Climate Change*, 2007, and references therein], aerosol-induced perturbations in mixed phase continental clouds and rainfall are still uncertain.

Investigations examining the short-term (2–3 h) effects of aerosols on convective clouds showed that increased CCN number concentration caused decreased precipitation amounts [*Teller and Levin*, 2006]. However, simulations of longer duration storms lasting ~12 h or more showed that the precipitation trend can reverse (i.e., produced more precipitation in an environment with more CCN) because of feedbacks on the storm dynamics [*van den Heever et al.*, 2006]. Other studies suggested that depending on environmental conditions, wind shear, aerosol, and cloud types [*Khain et al.*, 2008; *Fan et al.*, 2009; *Levin and Cotton*, 2008], aerosol-induced impact can either increase or decrease surface rainfall by more than 100% [*Tao et al.*, 2012]. A long-term simulation over Germany indicates that clouds may themselves act as natural buffers in large-scale cloud systems resulting in insignificant aerosol-induced change in overall surface precipitation

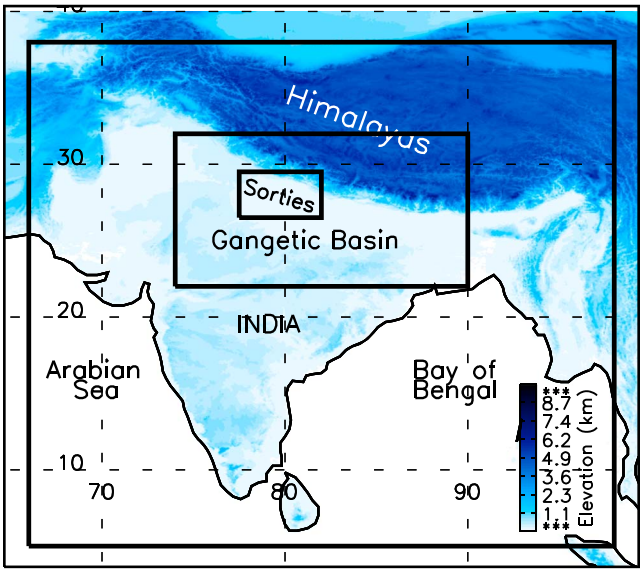

Figure 1. An overview map showing the CAIPEEX sortie region within Gangetic Basin of India and the nested domains used in model simulation. Shade represents the terrain height.

[*Seifert et al.*, 2012]. Many of these previous studies analyzed convection over North America and Europe. Here, we address aerosol-cloud-rainfall associations in convective cloud systems over the highly polluted North Indian Gangetic Basin using numerical simulations.

A major portion (about 45–50%) of summer monsoonal rainfall over Northern India occurs from Mesoscale Convective Systems (MCS) associated with monsoon depressions/lows [*Yoon and Chen*, 2005]. Monsoon depressions are generally formed in the Bay of Bengal (BoB) and propagate across the Indian landmass in a westward or north-westward direction with a life span of 4 to 6 days and at a speed of approximately 5° longitude/day. The MCSs associated with these depressions consist of deep, mixed phase convective clouds spread over an area of 2000–2500 km^2 [*Riehl*, 1971; *Daggupaty and Sikka*, 1977; *Sikka*, 1977; *Krishnamurti and Bhalme*, 1976]. The Gangetic Basin (GB), located in Northern India (Figure 1), is the most populated river basin in the world. Livelihood of about 600 million people in the GB is directly or indirectly dependent on agriculture and thereby on Indian monsoonal rainfall. In the last three decades, growth in industrialization and population density has turned the GB into a hot spot of anthropogenic pollution [*Dey and Di Girolamo*, 2011]. The association of local anthropogenic aerosol and the MCSs over the GB is not clear, primarily due to lack of measurements of colocated aerosol and cloud microphysics in this region.

In this paper, two questions are addressed. (1) How does propagation of these MCSs across northern India affect the prevalent regional aerosol concentrations? and (2) Is there any significant impact of local anthropogenic aerosol on cloud microphysics associated with such synoptic scale-driven MCSs? Answers to these questions will reduce the uncertainties in estimating the impact of anthropogenic CCN on cloud and rainfall during Indian monsoon.

During the monsoon period of 2009, colocated cloud microphysics, moist thermodynamics, and aerosol/CCN properties over different regions of India were measured by aircraft sorties during the Cloud Aerosol Interaction and Precipitation Enhancement EXperiment (CAIPEEX) campaign (http://www.tropmet.res.in/caipeex/). Two sorties (23 and 25 August) were conducted over the GB during the propagation of a typical monsoon depression event between 23 and 29 August 2009 over Northern India. In this study, the online chemistry coupled version of Weather Research and Forecasting (WRF) regional model, commonly known as WRF-Chem [*Skamarock et al.*, 2008; *Grell et al.*, 2005], which is capable of simulating aerosol direct and indirect feedbacks to address the complex aerosol-meteorology-cloud associations [*Fast et al.*, 2006; *Chapman et al.*, 2009; *Gustafson et al.*, 2007], is used to understand the aerosol-cloud associations over the GB during the 23–29 August monsoon depression event. A detailed discussion of the model configuration and various data sets used in this study is provided in section 2.

While *Kumar et al.* [2012b, 2012a] have evaluated WRF-Chem simulated meteorology and chemistry fields over India, the microphysical evaluation of WRF-Chem during summer monsoon over India has yet to be addressed. *Yang et al.* [2011] and *Saide et al.* [2012] have evaluated WRF-Chem microphysics comprehensively for marine stratocumuli over the Pacific Ocean using VOCALS-Rex campaign data. Similar to these previous studies, CCN and cloud microphysical properties in the Indian monsoon period must first be evaluated to gain confidence in the model's ability to simulate the complex aerosol and cloud processes. Hence, in this study, the model is first evaluated against in situ aircraft measurements of colocated aerosol, moist thermodynamics, and cloud microphysical profiles from CAIPEEX along with satellite observed aerosol and cloud optical properties and in situ measured accumulated surface rainfall (section 3).

The study addresses the two questions in sections 3 and 4, respectively. The effect of propagating MCSs on aerosol concentration over North India is discussed first (section 3.2), showing that aerosol concentration quickly replenishes after passage of MCSs. By using an aerosol sensitivity simulation with increased anthropogenic emission rates over the GB, the impact of aerosol on cloud properties including cloud physical processes is analyzed (section 4). The conclusions of the study (section 5) suggest that aerosols invigorated convective clouds during the CAIPEEX sorties over the GB.

2. Model and Measurement Details

2.1. Model Setup Details

We have configured WRF-Chem (version 3.5.1) to simulate the regional weather prevalent over India using three domains (Figure 1) from 20 to 29 August 2009. The outermost domain has 27 km resolution and covers the south Asian region, while the middle domain over Northern India has 9 km resolution. The innermost domain with a grid resolution of 3 km was centered around the region of CAIPEEX flights to resolve clouds explicitly. There are 34 layers between the surface and 50 hpa. The vertical structure of model was such that the region from the surface to the 1.5 km was represented by eight layers with vertical resolution of about 200 m, while the region between 1.5 and 3.5 km was represented by five layers with vertical resolution of about 400 m. Above 3.5 km, the vertical resolution was coarser at 800–1000 m. While this is a rather coarser vertical resolution for simulating convective clouds, 34 layers allowed simulations to be completed within our computational limitations. The National Center for Environmental Predictions (NCEP) Final Analysis (FNL) fields available at a resolution of 1°×1°and every 6 h provided the initial and lateral boundary conditions for the meteorological fields. As NCEP provided coarse initial and boundary conditions (IC/BC), the nested simulation with a South Asia domain at 27 km was used for better interpolation and simulation of the large-scale dynamics and physics that were fed into the inner domains as boundary conditions. The middle domain acted as a bridge connecting the coarser domain to the finer-scale domain. A spin-up time of 3 days was used for this two-way nested simulation.

Horizontal and vertical advection of winds, temperature, water vapor, cloud particles, trace gases, and aerosols were accomplished by the dynamical core of the model using a positive [*Janjic*, 2002] definite, monotonic scheme [*Wang et al.*, 2009]. The Mellor-Yamada-Janjic boundary layer scheme [*Janjic*, 2002] was used to parametrize the vertical subgrid-scale fluxes due to eddy transport in the planetary boundary layer and the free troposphere. The Noah land surface model was used to parametrize the surface energy balance [*Chen and Dudhia*, 2001]. The outer and middle domain used the Grell-Freitas cumulus parametrization scheme [*Grell and Freitas*, 2014]. The 30 min Moderate Resolution Imaging Spectroradiometer (MODIS) data set provided static geographical fields, such as terrain height, soil properties, vegetation fraction, land use and albedo, which were interpolated to the domain grids by using the WRF preprocessing system. To better analyze the aerosol-cloud interactions, nudging was not used in the simulations.

The model configuration used in this study (Table 1) can simulate the aerosol indirect effect. The Morrison microphysics scheme calculates the tendency of number and mass mixing ratios of cloud water, ice, snow, rain, and graupel. The size distributions of cloud droplets are represented by a gamma distribution, and all other hydrometeor species are expressed using an exponential function [*Morrison and Pinto*, 2005; *Morrison et al.*, 2009]. The interactions between clouds and shortwave radiation for the *first indirect effect* are implemented by linking the predicted cloud water and a constant effective radius from the Morrison cloud microphysics scheme with the Goddard shortwave radiative scheme. The Rapid Radiation Transfer Model (RRTM) scheme was used for longwave radiation [*Mlawer et al.*, 1997]. Activation of interstitial aerosol to droplet from each bin depends on the maximum supersaturation, which, in turn, is governed by vertical velocity, turbulent motions, and the internally mixed aerosol properties [*Abdul-Razzak and Ghan*, 2002]. During the activation process,

Table 1. Details of Various Parametrization Modules and Emission Inventories Used in the Simulation

Parameterizations	Module Used in Simulation
Land Surface Model	NOAH
Microphysics	Morrison double moment
Cumulus	Grell-Freitas
Planetary boundary layer	Mellor-Yamada-Janjic
Radiation	RRTM and Goddard shortwave scheme were used for long- and shortwave radiation calculations, respectively
Gas-chemistry module	CBMZ
Aerosol module	MOSAIC 4 bin module
Vertical layers	33
Domain resolution	27 km-9 km-3 km
Simulation time	10 days (20–29 Aug) (spin-up 3 days)
Anthropogenic emission inventory	MACCcity global emissions (2010) and INTEX-B emissions for PM2.5/10
IC/BC (chemistry)	MOZART global model runs
IC/BC (meteorology)	Reanalysis FNL (outer domain)
Static field	MODIS 20 category land use
Biogenic emission inventory	MEGAN online model (2009)

activated aerosols that form cloud droplets are removed from the aerosol spectra and added to the cloud droplet spectra. The ratio of the activated aerosol number concentration to the time step is considered as the activation rate and incorporated into the tendency budget of cloud droplets [*Wang et al.*, 2013]. Hence, the *second indirect effect* is estimated directly by the microphysics scheme as the number of activated particles affects precipitation and cloud lifetime.

The Carbon-Bond Mechanism modified by *Zaveri and Peters* [1999] (CBMZ) gas-phase chemical mechanism with dimethyl sulfide reactions was coupled to the four-bin sectional aerosol module, Model for Simulating Aerosol Interactions and Chemistry (MOSAIC) [*Zaveri et al.*, 2008], to simulate gases and aerosols. *Eidhammer et al.* [2014] found that the aerosol-cloud interactions represented by four bins produced similar results to the eight-bin MOSAIC scheme. In this scheme, size distributions for both unactivated/interstitial and activated aerosols in the range 0.039μm to 10μm are represented with four bins whose upper dry diameters are 0.156μm (bin 1), 0.625μm, 2.5μm, and 10μm (bin 4). Anthropogenic emissions of carbon monoxide, oxides of nitrogen (NO_x), sulfur dioxide (SO_2), ammonia (NH_3), black carbon (BC), organic carbon, and nonmethane volatile organic compounds are taken from the Monitoring Atmospheric Composition and Climate (MACC) and CityZEN projects, commonly referred as MACCity emissions inventory [*Granier et al.*, 2011], and emissions for PM_{10} and $PM_{2.5}$ (particles with diameter less than 10 μm and 2.5 μm, respectively) are taken from the Intercontinental Chemical Transport Experiment Phase B (INTEX-B) inventory [*Zhang et al.*, 2009]. Biogenic emissions of trace species are calculated using the Model of Emissions of Gases and Aerosols from Nature (MEGAN) [*Guenther et al.*, 2006]. Sea-salt emission rates were estimated in MOSAIC using a modified version of *Gong et al.* [1997a, 1997b], while dust emission rates used a modified version of the *Shaw et al.* [2008] parametrization. The fire inventory from National Center for Atmospheric Research (NCAR) version 1 was used for emissions of trace species from biomass burning. [*Wiedinmyer et al.*, 2011]. Six-hourly output from the global chemical model MOZART-4 (Model for Ozone and Related Chemical Tracers, version 4) [*Emmons et al.*, 2010] was used as initial and lateral boundary conditions (IC/BC) for the chemical species.

2.2. Satellite, In Situ, and Reanalysis Data Sets Used

We have used various satellite and reanalysis data sets to compare the modeled synoptic scale meteorological variables. Moderate Resolution Imaging Spectroradiometer (MODIS) daily level 2 swaths from the AQUA satellite platform were used [*King et al.*, 2003]. Aerosol optical depth (AOD) and cloud optical thickness (COT) gridded data sets of 0.25°× 0.25°resolution were estimated from MODIS level 2 observations. The gridded data set of upper air wind circulation from ERA-interim reanalysis was used to evaluate the synoptic scale wind pattern. Details about this reanalysis product are provided in *Dee et al.* [2011]. AERONET (AErosol RObotic NETwork) is a global ground-based aerosol monitoring network. AOD retrievals by AERONET have an

Table 2. Variables Measured During CAIPEEX Sorties and Their Corresponding Prognostic Variables in WRF-Chem[a]

Variables	Instruments Used	Model Prognostic Variable
RH	Thermoset polymer sensor	Vapor mixing ratio
T	Rosemount 102DB1CB	Temperature
Liquid water content (LWC)	CDP (2 μm–50 μm)	Cloud mass mixing ratio
Cloud droplet number	CDP	Cloud number concentration
Cloud droplet effective radii	CDP	Cloud droplet effective radius
Aerosol number concentration	PCASP (0.1 μm–3 mm)	(42% of bin1 + bin2 + bin 3)
Cloud condensation nuclei concentration (CCN)	CCN counter	CCN

[a]The acronyms CDP and PCASP denotes Cloud Droplet Probe and Passive Cavity Aerosol Spectrometer Probe, respectively.

uncertainty of approximately ±0.01 at 500 nm [*Eck et al.*, 1999]. AERONET measurements at Indian Institute of Technology, Kanpur (IITK) were used to compare modeled and measured AOD. Satellite estimates of 3-hourly gridded (25 km resolution) rainfall rate from Tropical Rainfall Measuring Mission (TRMM) were used to estimate accumulated rainfall to evaluate the spatial distribution. In situ surface rainfall gridded data set (25 km resolution) from the Indian Meteorological Department was also used to evaluate modeled rainfall between 23 and 29 August 2009. Black carbon (BC) and CCN concentrations at the surface are evaluated with measurements taken at IITK. The BC mass concentration was measured using a portable Aethalometeor (AE-31, Magee Scientific), while the CCN measurement was obtained from Droplet Measurement Technology (DMT) continuous-flow streamwise thermal-gradient CCN counter (CCN-100). The measurements of BC and CCN concentration were available during 22–26 August 2009 and were averaged every 4 h to compare with the corresponding simulated variables from WRF-Chem runs.

2.3. CAIPEEX Campaign

The aircraft campaign, CAIPEEX phase I, was conducted by the Indian Institute of Tropical Meteorology (IITM) during the 2009 monsoon (http://www.tropmet.res.in/caipeex/). In order to schedule CAIPEEX sorties, forecast and analysis of synoptic weather were used to select a region within the Indian landmass that had a high probability of formation of cumulus cloud. The major flight objectives were to simultaneously measure aerosols, CCN, cloud parameters, and large-scale meteorological conditions in and around cumulus clouds to develop an understanding on aerosol-cloud-rainfall associations over India [*Kulkarni et al.*, 2012]. CAIPEEX provided the only available simultaneous measurements of aerosol, cloud, and meteorology near cumulus clouds over the GB. In this campaign, an instrumented aircraft (Piper Cheyenne model PA-31 T) certified for flying into known icing conditions was used. Table 2 shows the specifications of instruments used and the variables measured during CAIPEEX sorties. It also lists the prognostic variables from WRF-Chem that are comparable with the measurements.

The observations were screened to retain the measurements when the flight roll angle and pitch angle were within ±20°. The Droplet Measurement Technology (DMT) Cloud Droplet Probe (CDP) was used to measure cloud droplet spectra of number concentration for fixed cloud droplet size bins within the range of 2 μm to 50 μm. Liquid water content (LWC) of cloud droplets was calculated from the measured droplet spectra. In determining cloud passes for analysis, data were restricted to times when LWC > 0.01 g m^{-3} and cloud droplet number concentration > 20 cm^{-3}. Moreover, a cloud pass consisted of continuous cloud measurement for more than 5 s under level flight conditions.

The DMT-CCN counter was operated between 0.1 and 1.2% supersaturation and measured a range of particles with radius within 0.5 μm to 10 μm [*Kulkarni et al.*, 2012]. In this study, we have considered the measurements made only at 0.2% supersaturation (1914 and 1572 samples during Sor23 and Sor25, respectively) for comparison between measured and modeled CCN concentration (also at 0.2%). The DMT SSP-200 Passive Cavity Aerosol Spectrometer Probe (PCASP) sampled aerosol number concentration in 30 size bins for the range 117 nm to 3 μm. To compare the measured and modeled aerosol number concentration, we have integrated the values from model bin numbers 2 and 3 (0.156 μm to 2.5 μm) with 42% of model bin number 1 (following *Saide et al.* [2012]). All aerosol measurements during level flight conditions except for the cloud passes were used to estimate the mean aerosol profiles. To compare measured and modeled $dN_{c,aer}/dlnDp$ values per size bin, the PCASP $dN_{c,aer}/dlnDp$ data from bins within the upper and lower

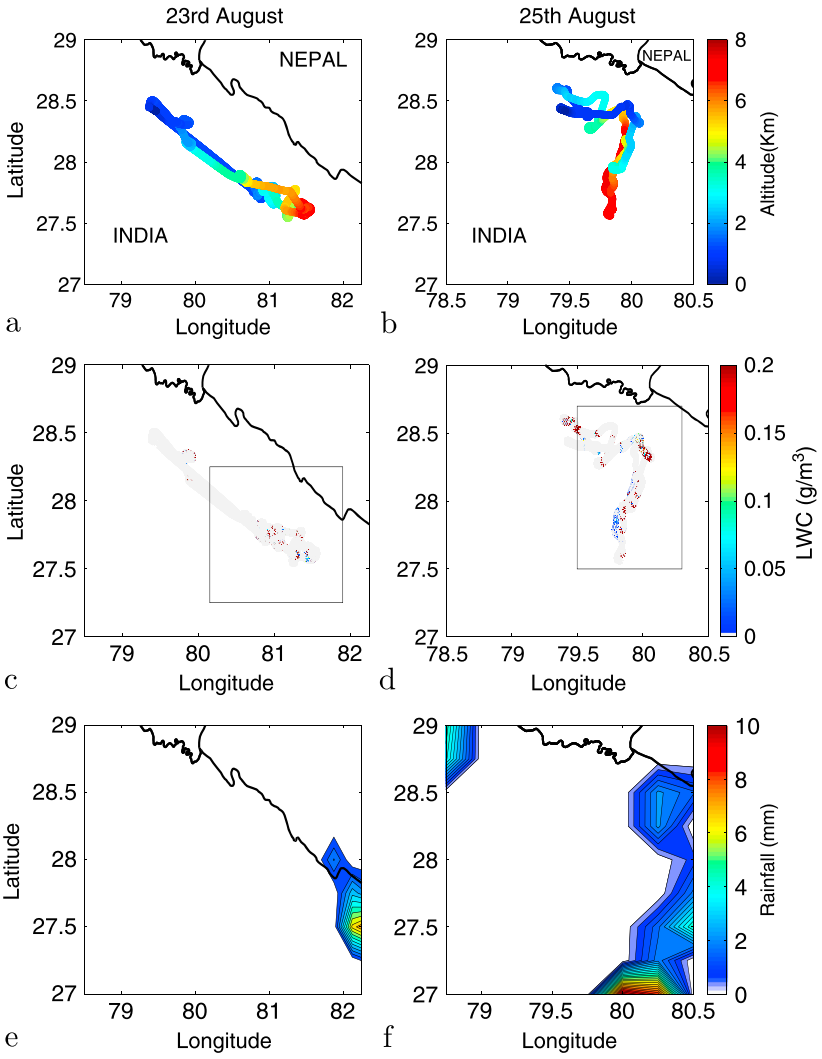

Figure 2. Variation in altitude of the two CAIPEEX sorties on (a, c, e) 23 August and (b, d, f) 25 August, respectively. Similarly, Figures 2c and 2d show variation in liquid water content (LWC), and Figures 2e and 2f illustrate corresponding accumulated rainfall (0600–1500 UTC) from TRMM for the two sorties. The regions marked by boxes in Figures 2c and 2d are used for representing mean profiles.

dry diameter of each MOSAIC size bin were summed to create $dN_{c,aer}/dlnDp$ values corresponding to the model size bins. The $dN_{c,aer}/dlnDp$ measurements and the model output were averaged spatially over the analysis region (marked by box in Figure 2) for altitudes below 2 km and temporally for the 0800 to 1400 UTC time period.

Figure 2 shows the aircraft flight paths on 23 and 25 August 2009 that are colored by altitude. The aircraft measured instantaneous LWC and TRMM accumulated rainfall (0600–1500 UTC) are also shown in Figure 2. Hereafter, we refer the sorties on 23 and 25 August as Sor23 and Sor25, respectively. During Sor23, the aircraft flew out of Bareilly airbase (28.4°N and 79.4°E) at about 9 UTC, into the cloudy region ahead of an approaching warm front south-east of Bareilly. The aircraft flew to the southeast till 27.5°N and 81.5°E. It ascended gradually from 9:30 UTC till 10:15 UTC where it sampled a convective cloud system. The aircraft spiraled down to the boundary layer and captured vertical variability of cloud properties. The flight flew back at an altitude of 2 km following the same diagonal path, reaching Bareilly at 11:30 UTC.

On 25 August 2009, the TRMM rain rate and the aircraft measured LWC show that the flight region was mostly cloud covered during the period of flight. The aircraft flew eastward from Bareilly airbase at around 9 UTC keeping the flight altitude below 2 km. The aircraft sampled a cloud system (below 2.5 km altitude) near 28.3°N and 80.1°E and then flew southwestward, adjacent to 80°E longitude, between 9:20 UTC and 10 UTC.

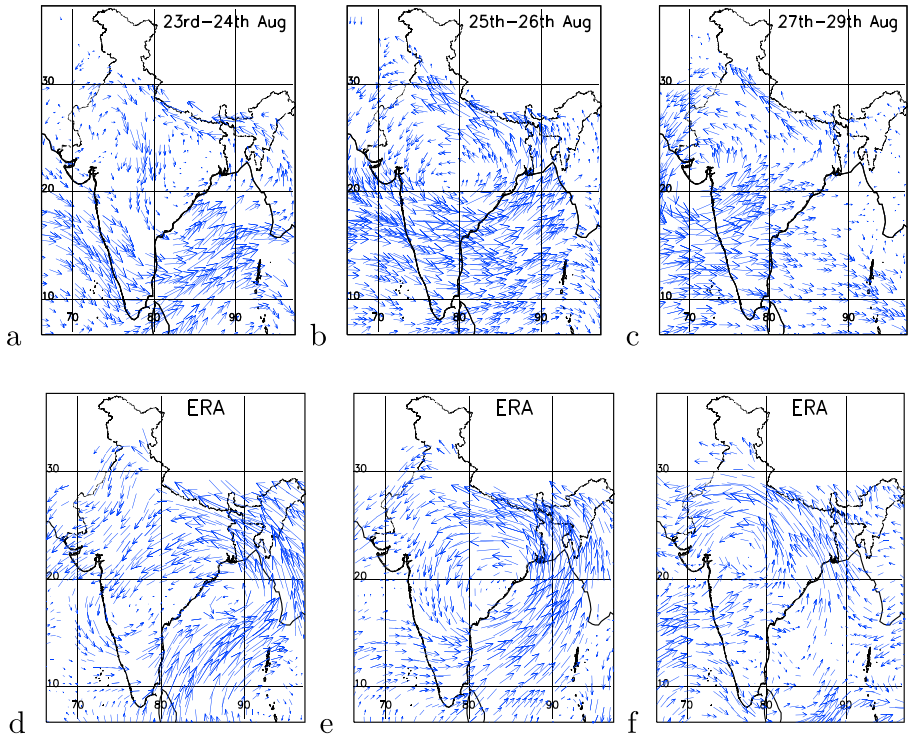

Figure 3. (a–c) Domain 1 simulated and (d–f) ERA reanalysis mean wind circulation at 850 hpa. Full arrows represent 10 m s^{-1}. The three columns represent temporal phases of monsoon depression 23–24 August (Figures 3a and 3d), 25–26 August (Figures 3b and 3e), and 27–29 August 2009 (Figures 3c and 3f), respectively.

It gradually ascended from 2 km altitude near 28.3°N till it reached 7 km altitude near 27.5°N sampling through cloud patches present at different altitudes. Then it turned back to the north and flew horizontally at high altitudes to reach the location near 28.3°N and 80.1°E (where low clouds were sampled earlier) and turned west, descending gradually through a few scattered cloud patches (at different altitudes) till it reached back to Bareilly airbase (Figure 2).

While Sor23 measured a convective tower cloud system by sampling in and out of cloud at different altitudes, a system of cumulus clouds developing at different altitudes was sampled during Sor25. The region bounded by boxes (Figure 2) in both the sorties was used to calculate mean profiles (details are given in the following sections), representative of the mean thermodynamical and microphysical fields.

3. Model Evaluation: Meteorology, Aerosol Distribution, and Microphysical Profiles

3.1. Meteorology and Thermodynamics

Using the outermost domain results, Figure 3 compares the simulated daily mean wind circulation pattern (at 850 hPa) and surface pressure with ERA-interim reanalysis data. The wind vectors show a prevalent cyclonic event over India during this period. The study period was divided into three temporal phases, 23–24 August, 25–26 August, and 27–29 August, representing different phases of the cyclone propagation. The ERA reanalysis data set shows that the winds over peninsular India were blowing eastward from the Arabian Sea toward BoB, while mostly easterlies blew over the GB. During 23–24 August, the depression was centered mostly over eastern India (19°N, 88°E). In the second phase, 25–26 August, the center of monsoon depression was located over central Indian region (19°N, 83°E). During 27–29 August, the monsoon depression propagated farther west and was centered over western India (22°N, 74°E). This westward propagation of synoptic-scale cyclones into India is a typical phenomena during the advent of monsoon depressions [*Sikka*, 1977; *Krishnamurti and Bhalme*, 1976]. Comparison of WRF-Chem winds in outer domain and ERA reanalysis data (Figures 3a–3c and 3d–3f, respectively) shows that WRF-Chem was able to simulate the cyclonic wind pattern, its spread and its westward propagation across India, but the simulated location of the center of the cyclone over the Indian landmass was to the northwest of the ERA observed monsoon depression center. Although, the simulated wind speeds over the Arabian Sea and the Western Ghats were higher than ERA reanalysis, the simulated wind

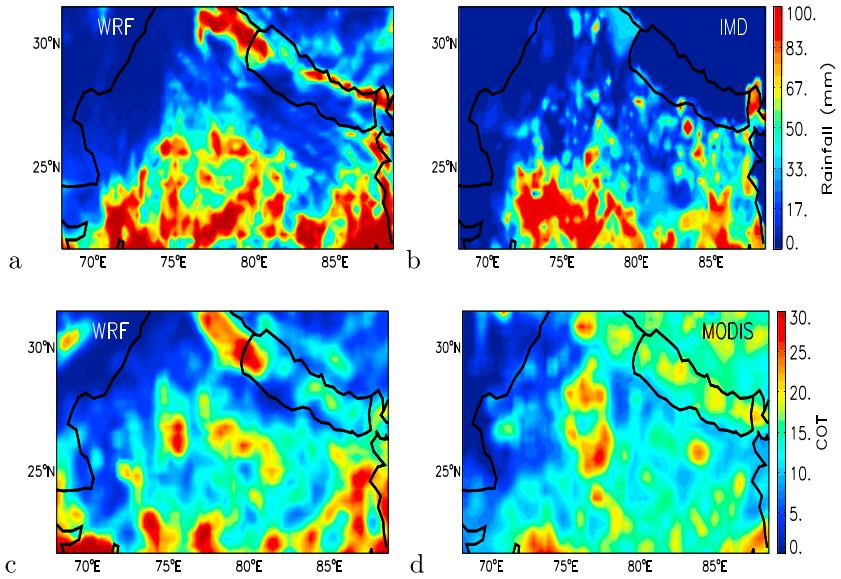

Figure 4. (left column) WRF-Chem and (right column) measurements of spatial distribution of (top row) accumulated rainfall and (bottom row) mean COT during 23–29 August.

speeds over the BoB and the GB were more similar to the reanalysis. Over the GB, the winds blew toward the northwest during all the three phases, which is well replicated by the model. However, the simulated wind speeds over the GB during phases 1 and 3 were less than ERA wind speed. Our comparison of WRF-Chem with the CAIPEEX wind measurements also shows this underprediction (discussed below). Because the WRF-Chem simulation was conducted as a continuous 9 day run, without data assimilation or reinitializations, it is not surprising that the modeled wind pattern does not exactly match with reanalysis observations.

WRF-Chem simulated surface rainfall (at 27 km resolution) and mean COT (corresponding to MODIS pass, 23–29 August 2009) are compared with accumulated gridded (25 km resolution) rain gauge measurement from Indian Meteorological Department (IMD) and MODIS retrievals (25 km resolution), respectively. Both simulated and observed rainfall show that heavy rainfall was concentrated over southern and southeastern part of the GB in both simulated and observed data (Figure 4). The widespread rainfall over southeastern parts is also a characteristic of a typical monsoon depression propagation during Indian summer monsoon [*Sikka*, 1977; *Krishnamurti and Bhalme*, 1976]. WRF-Chem was able to simulate the general rainfall and cloud distribution but with some differences in absolute magnitude and distribution. Over the mountainous region (near 30°N 79°E), the model overestimated rainfall and COT compared to the observations but underestimated the rainfall values for the scattered cloud structures between 25°–27° N and 83°–86°E. The differences in observed and simulated meteorology and rainfall can be attributed to the coarse model resolution, uncertainties associated with the physical parametrizations (mainly the cumulus parametrization), and the errors propagation (in space and time of temperature, pressure, winds, and moisture) during the 9 day long continuous run. Further, the lower density of in situ IMD measurement sites (used to make the gridded data set) in the mountainous and rural regions of Northern India may be missing localized rainfall events thereby contributing to these differences. Previous regional modeling studies have shown similar differences in observations and simulated meteorology during summer monsoon period, and specifically during monsoon depression period [*Venkata Ratnam and Cox*, 2006; *Potty et al.*, 2000; *Kumar et al.*, 2012a; *Routray et al.*, 2014].

Vertical profiles of temperature (*T*), relative humidity (RH), and horizontal wind speed (HWS) simulated by WRF-Chem and averaged spatially in the CAIPEEX region (boxes in Figure 2) and temporally for 0800–1400 UTC are evaluated with the CAIPEEX aircraft data, which have also been averaged spatially and temporally (Figure 5). The mean of measured value of the variables along with the bias (model-observed) in corresponding WRF-Chem simulated variables is given in Table 3. Correlation coefficients (*R*) which were significant at 95% confidence interval are also calculated to quantify the similarity in vertical gradients of measured and modeled variables.

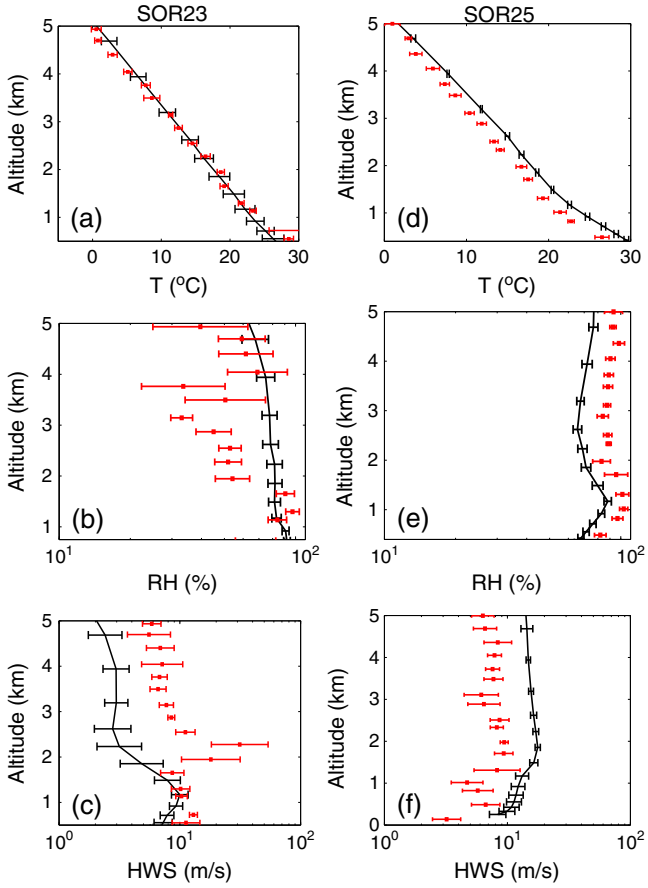

Figure 5. Comparison of measured (red) temperature (*T*), relative humidity (RH), and horizontal wind speed (HWS) values with WRF-Chem-simulated values (black) during (a, b, c) Sor23 and (d, e, f) Sor25, respectively.

Table 3 shows that mean observed *T* (11.3°C) was slightly underestimated during Sor23. Simulated HWS and RH were close to their observed values below 2 km, but RH was overestimated between 2 and 4 km altitude and HWS was underestimated by ~5 m s^{-1} above 2 km. The high bias in simulated RH and HWS between 2 and 4 km caused low correlation ($R = 0.34$ and 0.3, respectively) for these two parameters, but *T* was well correlated ($R = 0.99$). For Sor25, WRF-Chem overestimated observed mean *T* (11.8°C) and HWS (8.4 m s^{-1}) by 1.7°C and 6.7 m s^{-1}, respectively, and underestimated mean RH (92%) by 18%. During Sor25, the correlation coefficients for *T*, RH, and HWS were found to be 0.99, 0.9, and 0.8, respectively, indicating (as also visible in Figure 5) that the observed vertical gradients were well simulated by the model. The mean absolute errors (average of two sorties) in simulated RH, HWS and *T* were found to be ~15%, ~6 m s^{-1} and ~0 5 K, respectively, which are comparable with previous model-observation comparison studies. For example,

Table 3. Volume (0.5–5 km Altitude Over Volume (From Surface to 5 km Altitude Over the Analysis Box in Figure 2) and Temporally Averaged (0800–1400 UTC) Mean Values of Measured Temperature, Relative Humidity, and Horizontal Wind Speed for Both Sorties and the Corresponding Bias (Model-Measurement) in Base WRF-Chem Simulation[a]

Sortie	Variable	CAIPEEX Mean	WRF-Chem Bias	Correlation coefficient (*R*)
SOR23	*T* (°C)	11.3	−0.3	0.99
	RH(%)	64	15.5	0.34
	HWS (m/s)	9.8	−5.7	0.29
SOR25	*T* (°C)	11.8	1.7	0.99
	RH (%)	91.9	−18	0.89
	HWS (m/s)	8.4	6.7	0.81

[a]Correlation coefficient (*R*) between measured and modeled values.

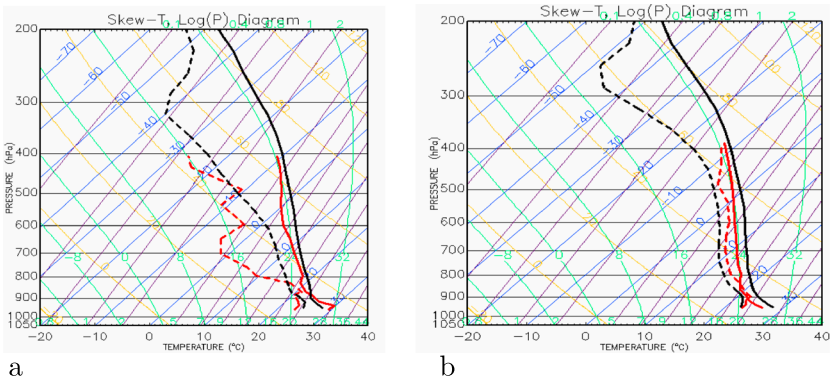

Figure 6. Skew *T* diagram representing moist thermodynamical condition during CAIPEEX (red) and modeled (black) sorties on (a) 23 and (b) 25 August 2009. Solid lines represent temperature profiles, and dashed lines represent dew point temperature.

in *Misenis and Zhang* [2010], aircraft measurements made during Texas Air Quality Study near Houston were used to compare WRF-Chem simulated vertical profiles of *T* and RH. The range in biases of RH and *T* was 0–25% and 0–1 K, respectively. *Chandrasekar et al.* [2003] also showed that the mean relative error in RH was in the range of 10–50%, and in the range of 0–2.2 K in *T*. Similar comparison over Iceland also found biases of 25% and 2 K in modeled RH and T [*Mayer et al.*, 2012]. Further, in agreement with *Cox et al.* [1998], Figure 5 also illustrates that the model error for thermodynamic variables was higher at higher altitudes. *Cox et al.* [1998] had compared four regional models in their study (including Regional Atmospheric Modeling System (RAMS) and MM5 (short for Fifth-Generation Penn State/NCAR Mesoscale Model) community model) and illustrated that these models had difficulty in accurately predicting upper air dew point field. They suggested this error may be caused by the lack of upper level moisture observations in a particular region which leads to difficulty in accurately initializing dew point.

It was observed that the mean moist thermodynamic conditions prevalent over the GB during Sor23 and Sor25 were very distinct (Figure 6). Very humid conditions were prevalent over the GB during Sor25, while comparatively drier conditions were prevalent during Sor23. Spatial (area bounded by the black box in Figure 2) and temporal (0800–1400 UTC) mean convective available potential energy (CAPE) for both sorties were calculated from observed and simulated mean *T* and RH profiles. Mean CAPE calculated from observed profiles during Sor25 (=1250 J/kg) was less than CAPE (=2900 J/kg) during Sor23. The onset of rainfall in phase 1 over CAIPEEX region expended CAPE causing the decrease in convective activity in phase 2. The WRF model was able to simulate the magnitude of CAPE during Sor25 (= 1208 J/kg) and Sor23 (= 3200 J/kg) reasonably well. Although the errors in WRF-Chem simulated *T* and RH were high at higher altitudes, the simulation captured the moist thermodynamics conditions of Sor23 and Sor25 reasonably well.

The foregoing comparisons provide confidence that our simulations were able to represent not only the large-scale meteorological conditions, including cloud and rainfall distribution, but also the general trend in local scale moist thermodynamical conditions.

3.2. Evaluating Aerosol Distribution: Impact of Propagating Monsoon Depression

To evaluate WRF-Chem simulated aerosol fields and the impact of the monsoon depression propagating westward on the aerosol concentration over the GB, spatial aerosol distribution during the three phases of monsoon depression, 23–24 August, 25–26 August, and 27–29 August, were examined (Figure 7). Quality assured AOD retrievals by MODIS are not available over cloudy regions; thus, the missing grids are marked by white patches. During 23–24 August, the aerosol concentration in the GB, especially in the region of CAIPEEX flights (Domain 3 in Figure 1), was very high (AOD > 0.8). As the depression propagated toward central India during 25–26 August, mean AOD of the CAIPEEX region decreased to 0.2–0.3 (Figure 7b). Dilution of aerosol loading due to inflow of relatively clean marine air, cloud ingestion of aerosol by the approaching MCSs, and removal of aerosol by wet scavenging effect could be potential reasons behind this dramatic decrease in aerosol concentration between these two phases. In addition, the convergence of winds from opposing directions during the first phase of monsoon depression (Figure 3a) might have also fostered stagnation and thereby accumulation of aerosol during Sor23. However, rapid buildup of aerosol loading over

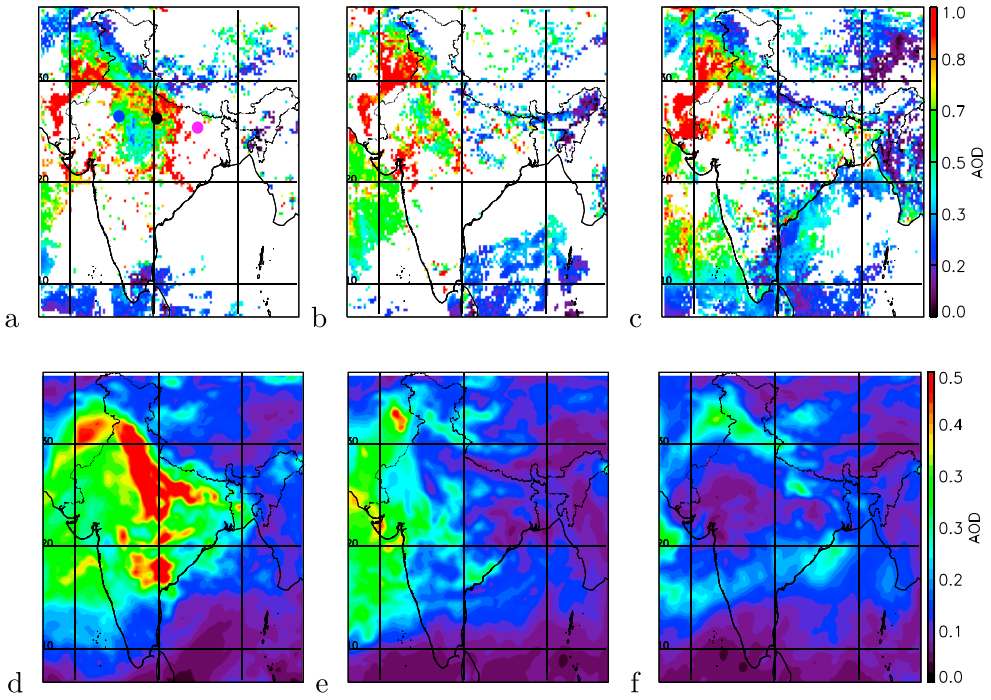

Figure 7. (a, b, c) MODIS-observed mean AOD distribution and (d, e, f) modeled mean AOD distribution from Domain 1, respectively. The three columns from left to right represent the temporal period of 23–24 August, 25–26 August, and 27–29 August 2009, respectively. The blue, black, and magenta dots in Figure 7a represent AERONET sites at Jaipur (JPR), Kanpur (KNP), and Gandhi College (GC), respectively. White patches in Figures 7a, 7b, and 7c denote missing AOD observations.

the CAIPEEX region was observed during 27–29 August as the MCS moved toward western India (Figure 7c). The WRF-Chem simulation was able to simulate the spatial and temporal variations in AOD but underestimated AOD (up to 50%) in magnitude compared to MODIS AOD. By comparing the measured instantaneous AOD values at three AERONET sites in the GB with simulated AOD values (from domain 2 interpolated to the time of AERONET measurements), the large underestimation of simulated AOD values is clearly seen for AOD < 0.45 (Figure 8a).

There could be a few reasons for simulating the spatial and temporal aerosol distribution well, but under predicting the magnitude of aerosol optical depth. The concentrations of aerosols used as the initial and boundary conditions, obtained from the global MOZART model, may be much lower than observations. However, a 3 day spin-up of WRF-Chem should remove the influence of the initial conditions in the boundary layer where most of the aerosol resides. The MOZART boundary conditions should have a minimal effect on the boundary layer aerosol concentration in the CAIPEEX region (domain 3 in WRF-Chem simulations), which is far away from the outer domain boundaries, but it may have larger effects above the boundary layer [*Kumar et al.*, 2015a]. The wet deposition of aerosols may be too excessive, reducing aerosol concentrations. However, a simulation performed with the same model configuration and emission rates over the same region, but for the premonsoon period (22–29 May 2009) when very little precipitation occurs, produced AOD values about 50% less than MODIS AOD. Therefore, it is likely that wet deposition is not substantially wrong. The emission rates of PM may be too low because the INTEX-B inventory represents 2006 emissions while we simulate 2009. In addition, there may be missing contributions from emission sectors, e.g., trash burning and fossil fuel-based cooking stove emissions, and other uncertainties from the compilation of emission data [*Wiedinmyer et al.*, 2014]. Although minor, the contribution from mineral dust emissions from Indian desert, which have considerable optical properties [*Mishra and Tripathi*, 2008], might also be underrepresented. Other modeling studies at both the global and regional scales have also shown large biases (factors of 3–8) in long-term comparisons of simulated BC and AOD over the Indian landmass (due to underrepresentation of the anthropogenic emission rates) using different emission inventories [*Ganguly et al.*, 2009; *Menon et al.*, 2010; *Nair et al.*, 2012]. A recent study using high-resolution emission inventory (10 km × 10 km) has shown much better evaluation of BC concentration over South Asia [*Kumar et al.*, 2015b]. Hence, the coarse resolution (40 km × 40 km) of the

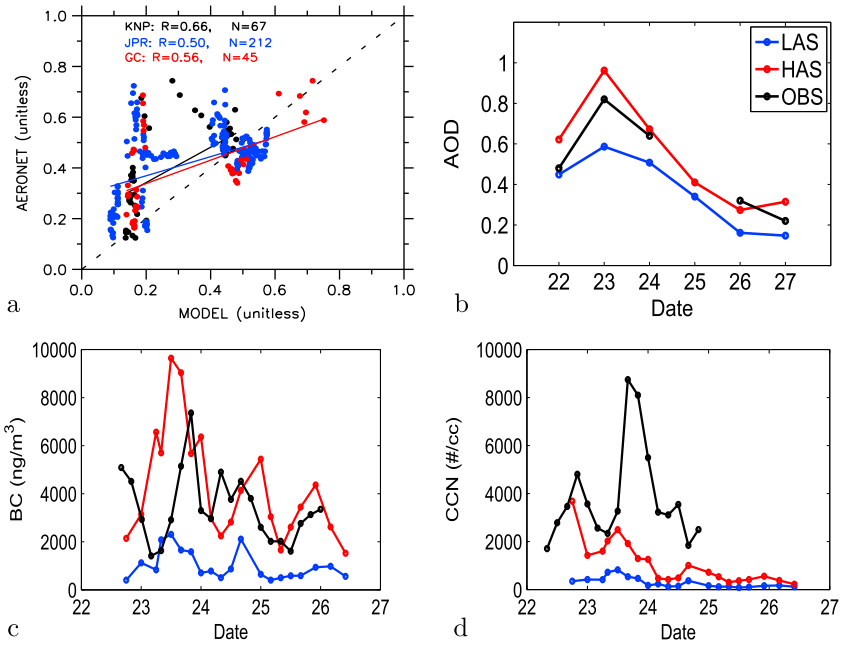

Figure 8. (a) AERONET-measured instantaneous AOD at three sites, Jaipur (JPR), Kanpur (KNP), and Gandhi College (GC) with simulated (low-aerosol scenario, LAS) AOD (interpolated to AERONET measurement time). The location of these sites are shown in Figure 7. (LAS (blue) and HAS (red) simulated mean ((b) mean daily) AOD, ((c) mean 4-h) BC, and ((d) mean 4-h) CCN, respectively, with corresponding measured values (black) at IIT Kanpur (IITK).

gridded global emission inventory used here may be an important factor contributing to the underestimation of aerosol concentrations.

In situ surface and columnar aerosol measurements over Kanpur (Figure 8) in central GB region as well as aerosol number concentration ($N_{c,aer}$) profiles measured during CAIPEEX sorties (Figure 9) were used to evaluate the performance of WRF-Chem when anthropogenic emission rates in the innermost domain (CAIPEEX region) were enhanced. After testing a few increased emissions, we found that aerosol fields in the innermost domain were better simulated when anthropogenic aerosol emission rates were increased by a factor of 6. Hereafter, the simulation with default MACCity+INTEX-B anthropogenic emission inventory is referred to as low-aerosol scenario (LAS) run, and the simulation with enhanced emission inventory is referred to as high-aerosol scenario (HAS) run.

Figure 8b compares AERONET-measured mean daily AOD at Kanpur with corresponding WRF-Chem simulated mean daily AOD from 23 to 27 August. In agreement with the temporal trend of MODIS-observed AOD, the time series (23–27 August 2009) of AERONET-measured daily mean AOD values also show decrease in aerosol loading (AOD) from 23 to 27 August. While the LAS simulation significantly underpredicted the AOD

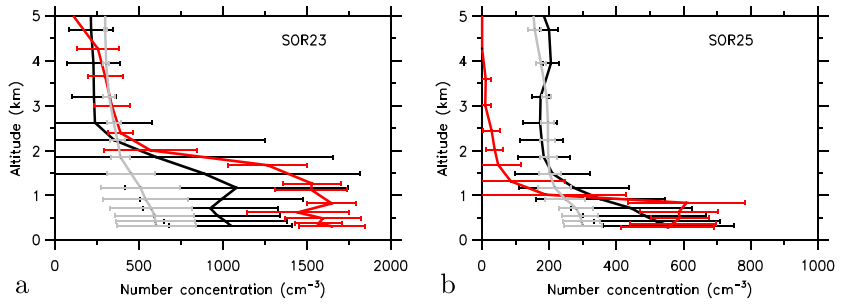

Figure 9. Vertical profile of aerosol number concentration for (a) Sor23 and (b) Sor25 averaged for clear sky. Red line is mean aircraft measurements averaged at midpoint of model domain vertical levels. Gray and black lines are WRF-Chem averages in the CAIPEEX region for LAS and HAS runs, respectively. The horizontal lines denote standard deviations.

values at Kanpur, the HAS simulated AOD values were about 0.4 greater than that from LAS runs and were similar to corresponding AERONET-measured mean daily AOD.

The measured BC and CCN concentrations also were high (maximum ~10000 ng m^{-3} and ~8000 cm^{-3}, respectively) between 23 and 24 August and decreased gradually till 26 August following the trend similar to observed AOD. The simulated black carbon (BC) mass concentration (Figure 8c) and CCN number concentration at 0.2% supersaturation (Figure 8d) from both runs were compared with measured BC and CCN concentration at IITK during the study period. Normalized root-mean-square error (NRMSE) was calculated by dividing root-mean-square error by mean observed data. The LAS run underestimated BC and CCN concentration by factors of 3–5. The time series and magnitude of BC concentrations simulated by HAS run were closer (NRMSE = 0.34) to the in situ measurement than LAS run (NRMSE = 0.43). Figure 8 shows that predicted CCN concentration improved in HAS (NRMSE = 0.44) compared to LAS run (NRMSE = 0.58). However, even with enhanced emission, the magnitude of CCN at surface was underestimated by factors of 2–4 compared to measurements.

WRF-Chem simulated vertical profiles of aerosol number concentration $N_{c,aer}$ averaged spatially (in the CAIPEEX region boxes in Figure 2) and temporally (0800–1400 UTC) are evaluated against the CAIPEEX aircraft measured profiles, which have also been similarly averaged spatially and temporally for both Sor23 and Sor25 (shown in Figure 9). During Sor23, $N_{c,aer}$ up to 1.5 km altitude was high (> 1000 cm^{-3}), while during Sor25 the $N_{c,aer}$ was three times smaller (500 cm^{-3}) at the same altitudes. The HAS simulated $N_{c,aer}$ had better agreement with the observations than the LAS run for both CAIPEEX sorties. The aircraft observations show that the aerosol concentrations is well mixed in the boundary layer with high-aerosol concentrations (Figure 9) that drop off steeply to lower concentrations in the free troposphere. This vertical gradient is replicated in the HAS simulation, in which more aerosols were emitted into the lowest model level (compared to LAS run) causing an accumulation of aerosol in the boundary layer. The difference in aerosol vertical distribution between LAS and HAS runs caused the differences in CCN near cloud base and thereby in cloud microphysics as discussed in section 4.

To show how the aerosol number size distribution changes between LAS and HAS runs, we plotted the mean $dN_{c,aer}/dlnDp$ values against mean diameter (Dp) of the three smallest model bins (Figure 10) along with PCASP average data (see section 2.3). Both observations and model results show that the aerosol number concentration was dominated by smaller particles. During Sor23, LAS simulated $dN_{c,aer}/dlnDp$ in bin 1 (bias= −800 cm^{-3}) was comparatively closer to the corresponding measured value (4190 cm^{-3}), but simulated value in bin 2 (bias = −2400 cm^{-3}) was underestimated against measured value (2790 cm^{-3}). Bias in HAS simulated $dN_{c,aer}/dlnDp$ in bins 1 and 2 was 1278 cm^{-3} and −1480 cm^{-3}, respectively. The predicted $dN_{c,aer}/dlnDp$ for Sor25 was similar with a bias in LAS (HAS) simulated $dN_{c,aer}/dlnDp$ in size bin 1 and bin 2 of 230 cm^{-3} (330 cm^{-3}) and −570 cm^{-3} (−430 cm^{-3}), respectively. The corresponding measured values for size bins 1 and 2 were 1715 cm^{-3} and 770 cm^{-3} , respectively. The $dN_{c,aer}/dlnDp$ for bin 3 in both sorties was comparatively negligible. Thus, it is inferred that the bias in $N_{c,aer}$ profiles was mainly due to underestimation of aerosol concentrations in size range below 0.625 μm. Increase in anthropogenic emission (HAS runs) reduced the bias of $dN_{c,aer}/dlnDp$ for $Dp < 0.625$ μm for both the sorties, thereby resulting in the HAS simulated $N_{c,aer}$ profiles being more similar to observations (Figure 9). Nevertheless, differences in the shape of aerosol number concentration spectra between LAS and HAS runs were negligible for both sorties.

In summary, as the MCSs associated with monsoon depression propagated westward from BoB over the Indian landmass, aerosol loading over the GB was reduced. However, as the depression moved farther westward, the aerosol concentration over the GB was replenished within a day or two. The WRF-chem prediction of AOD, BC concentration, and aerosol number concentration values in the innermost domain agreed reasonably with MODIS AOD, AERONET, surface measurements, and CAIPEEX profiles when anthropogenic emission rates were substantially increased. Thus, the MACCity+INTEX-B emission inventories may be underestimating actual emission rates, because of possible underrepresentation in the emission inventory and missing emission sectors.

3.3. Evaluating CAIPEEX Microphysical Profiles

Area- and time-averaged model and aircraft microphysical profiles of the sampled cloud system were compared. We assumed that the clouds sampled by the aircraft are representative of the clouds in the same area at the same time in terms of microphysical features. This permitted the observed microphysical variables along the flight paths to be statistically compared with area averaged model simulated microphysical

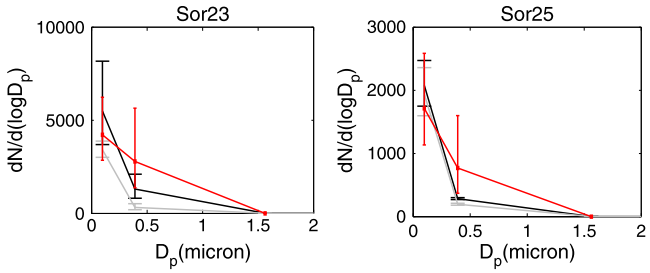

Figure 10. Measured (red) aerosol number distribution and corresponding predicted values from the LAS (grey) and HAS (black) simulations for (left) Sor23 and (right) Sor25, respectively. The error bars represent standard deviations. The fourth size bin is not shown because the measurements do not include the sizes >3 μm, and the number concentration is negligible compared to smaller size bins.

variables. Simulated vertical profiles of CCN at 0.2% supersaturation, liquid water content (LWC), droplet effective radius (R_e), and cloud droplet number concentration (N_c) averaged spatially in the CAIPEEX region (boxes in Figure 2 and temporally for 0800–1400 UTC are evaluated with the CAIPEEX aircraft data, which have also been averaged spatially and temporally for both Sor23 and Sor25. All the aircraft measurements within every 350 m layer from surface were averaged and plotted with their standard deviations at the corresponding mean height. NRMSE was calculated to quantify the performance of model runs. The mean and NRMSE values of the variables are reported in Table 4. The correlation coefficient (R) between mean model and measured mean values was also computed (significant at 95% confidence interval) to quantify the simulated vertical trends against observations.

During Sor23, the lower atmosphere had high CCN concentrations (1100 cm^{-3}) resulting in mean N_c of 360 cm^{-3}. In contrast, during Sor25 the CCN concentrations were less (480 cm^{-3}, respectively) producing N_c of ~100 cm^{-3}. Mean R_e values were 8.5 μm and 8.8 μm during Sor23 and Sor25, respectively. While CCN concentration and N_c decreased with height, R_e increased with height for both the sorties (Figure 11). Both LAS and HAS simulations predicted mean cloud properties that correlate well with the observations for Sor23. But the LAS run had considerably more bias compared to observations than the HAS run, indicating that the HAS run performed better for predicting cloud properties. Similarly, the mean concentration and the vertical distribution of CCN, N_c, R_e, and LWC during Sor25 (Figure 11) were also better simulated by HAS run as compared to LAS run (Table 4). However, the HAS model run still underestimated the N_c and LWC during both the sorties, especially at higher altitudes. N_c was underestimated by factors of 2–3, and LWC was underestimated by factors of 1–2 for both sorties. The gradient in R_e was simulated fairly well (R >0.95 for

Table 4. Volume (0.5–5 km Altitude Over Analysis Box in Figure 2) and Temporally Averaged (0800–1400 UTC) Mean Value of Measured and Simulated CCN Concentration, Droplet Number Concentration (N_c), Liquid Water Content (LWC), and Droplet Effective Radii (R_e) for Sor23 and Sor25[a]

Variables	CAIPEEX Mean	LAS Mean	HAS Mean	LAS NRMSE	HAS NRMSE	R (LAS)	R (HAS)
Sor23							
CCN (#/cm^3)	1100	370	780	0.47	0.30	0.54	0.60
N_c (#/cm^3)	360	58.3	148.8	1.1	0.67	0.62	0.84
R_e (μm)	8.5	11.1	9.2	0.41	0.25	0.97	0.98
LWC (g/m^3)	0.80	0.27	0.37	0.71	0.46	0.1	0.23
Sor25							
CCN (#/cm^3)	480	226	288	0.35	0.29	0.76	0.87
N_c (#/cm^3)	100.3	30.8	77.4	0.51	0.34	0.2	0.6
R_e (μm)	8.8	11.8	9.9	0.44	0.24	0.95	0.95
LWC (g/m^3)	1.07	0.39	0.71	0.57	0.41	0.2	0.35

[a]Calculated normalized root-mean-square error (NRMSE) and correlation coefficient (R) between measured and modeled value are also reported.

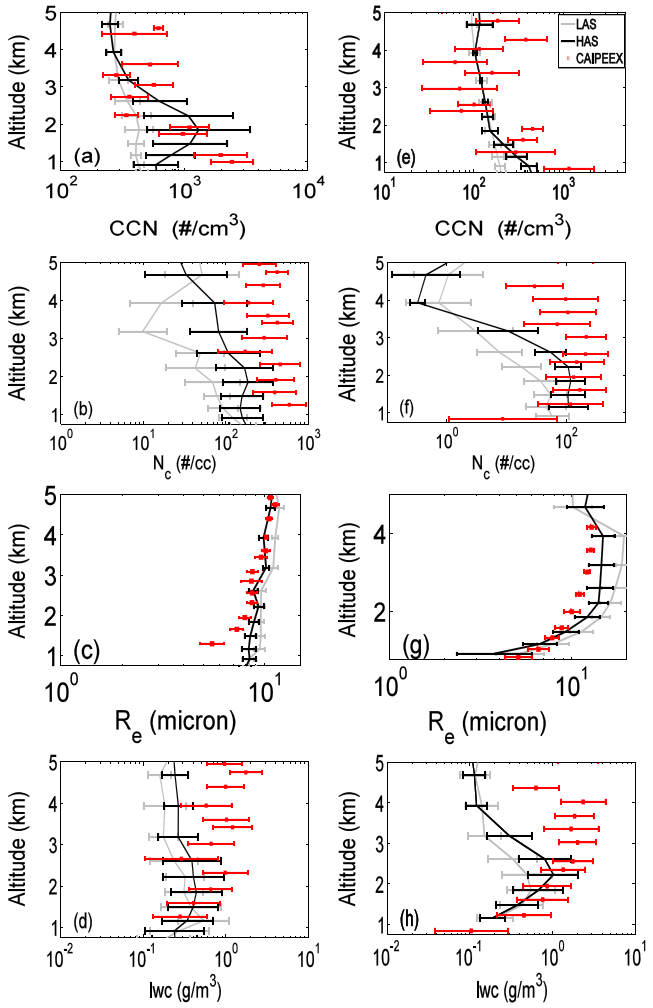

Figure 11. Observed and simulated mean vertical profiles of CCN, Cloud droplet number concentration, N_c, droplet effective radius (R_e), and liquid water content (LWC) for (a–d) Sor23 and (e–f) Sor25.

both runs), but R_e was overestimated at lower altitudes. Given that the performance of a numerical weather prediction model is dependent on initial conditions, resolution, physical parametrizations, etc., such quantitative comparison constitutes a very severe test. Previous studies comparing performance of various regional models have also reported similar biases in simulated cloud droplet properties [*Colle et al.*, 2005; *Zhang et al.*, 2007; *Shi et al.*, 2010; *Hazra et al.*, 2013].

In summary, the model was able to simulate the fundamental aerosol processes and thereby the observed vertical trends in the CCN values and cloud microphysical properties reasonably well ($R > 0.5$, except LWC) but had offset from observed magnitude for both sorties.

4. Aerosol-Cloud Interactions

Analyzing the differences in measured aerosol and cloud properties between Sor23 and Sor25 (Figures 9 and 11) shows an interesting feature. During Sor25 (mean CCN concentration is low), a fewer number of bigger cloud droplets were present per unit volume of air as compared to that in Sor23 (mean CCN concentration is high). As discussed above, the reduction in aerosol loading from 23 to 25 August coincided with the propagation of the monsoon depression. While an analysis comparing the measured aerosol and cloud properties between the two sorties could reveal aerosol effects on the clouds, it would not provide a sufficiently controlled experiment that could be done with the model results from the LAS and HAS simulations. Therefore, we analyze the two aerosol sensitivity runs to study the simulated impact of increase in local aerosol on cloud microphysics and dynamics for both Sor23 and Sor25 individually.

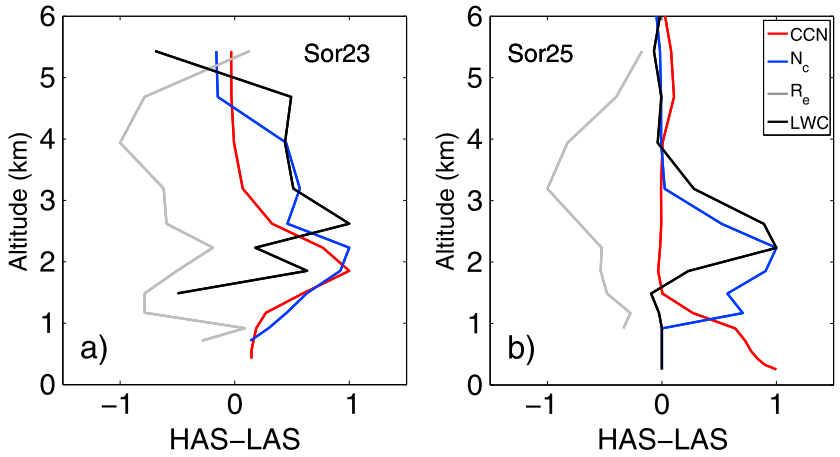

Figure 12. Spatial and temporal average vertical profiles of the difference (HAS-LAS) normalized to the maximum difference in simulated CCN (red), cloud number concentration (blue), cloud effective radius (gray), and liquid water content (black) for (left) Sor23 and (right) Sor25.

The meteorology in the HAS simulation is quite similar to that in LAS simulation. First, the aerosols in the outer model domains are not modified (except when air flows out of domain 3), because aerosol emissions are changed only in domain 3. The large-scale synoptic meteorology shows that the monsoon depression and associated winds are very similar in the LAS and HAS simulations. Specifically, the track of the monsoon depression is the same in the two simulations. As model parameters and meteorological conditions are similar, the differences in simulated cloud microphysics between HAS and LAS over domain 3 are mainly due to the differences present in the aerosol fields (Figures 8, 9, and 10) between the two simulations. By making horizontal averages within the analysis region (Figure 2) for comparison, differences due to spatial shift in location of simulated cloud systems among the two runs were minimized.

The differences (HAS-LAS) in simulated CCN, N_c, R_e, and LWC values of mean profiles for both Sor23 and Sor25 are shown in Figure 12. The differences at each layer were normalized with the maximum difference between 0 and 6 km to enable comparison of all the variables together in same plot. Cloud base (from aircraft measurements) was present ~ 1.2 km and ~ 0.7 km for Sor23 and Sor25, respectively [*Prabha et al.*, 2012, Table 1]. It was found that CCN concentration increased mostly between 0.8 km and 3 km during Sor23. In case of Sor25, the increase was mainly below 2 km. Compared to the LAS run, the HAS run simulated higher concentration of CCN in boundary layer for both the sorties. It was also found that HAS simulated N_c was greater (than LAS values) in lower part of cloud for both sorties, mainly between 1 km and 4 km. At the same altitudes, R_e values were found to be smaller in case of HAS run. Thus, under polluted condition (compared to clean condition), increase in N_c and decrease in R_e was found for both the sorties. Subsequently, the feedback resulted in increase in LWC or cloudiness under high-aerosol scenario. Similar aerosol-cloud association near cloud base, commonly referred as aerosol first indirect effect, has also been reported, mostly in warm clouds (discussed in section 1).

To investigate aerosol-induced perturbations on the vertical distribution of simulated hydrometeor species, we compared the COT, rainfall, and cloud hydrometeor mass concentrations from the HAS and LAS runs for both the sorties. For both Sor23 and Sor25, mean mass concentration profiles of simulated cloud droplet, raindrops, graupel, snow, and ice hydrometeors were calculated by spatially and temporally (0800–1400 UTC) averaging the respective values in only cloudy grids within our analysis boxes (shown in Figure 2). Figures 13a and 13b and 14a and 14b show the time series of COT and accumulated surface rainfall for both the simulations during Sor23 and Sor25, respectively. Further, Figures 13c–13h and 14c–14h compare the mean hydrometeor profiles at three time slices 0900 UTC (c and d), 1100 UTC (e and f) and 1300 UTC (g and h) for both Sor23 and Sor25, respectively. Figures 13c, 13e, 14g, 14c, 14e, and 14g represent mean profiles from LAS run, and Figures 13d, 13f, 13h, 14d, 14f, and 14h represent mean profiles from HAS runs.

The simulated maximum LWC during both the events was 1.2 g/m^3, near 2–3 km altitude. The model also simulated the presence of supercooled raindrops at much high altitudes (up to 10 km in some cases) above the freezing level (around 5.2 km). *Konwar et al.* [2012] have also reported the presence of supercooled droplets at

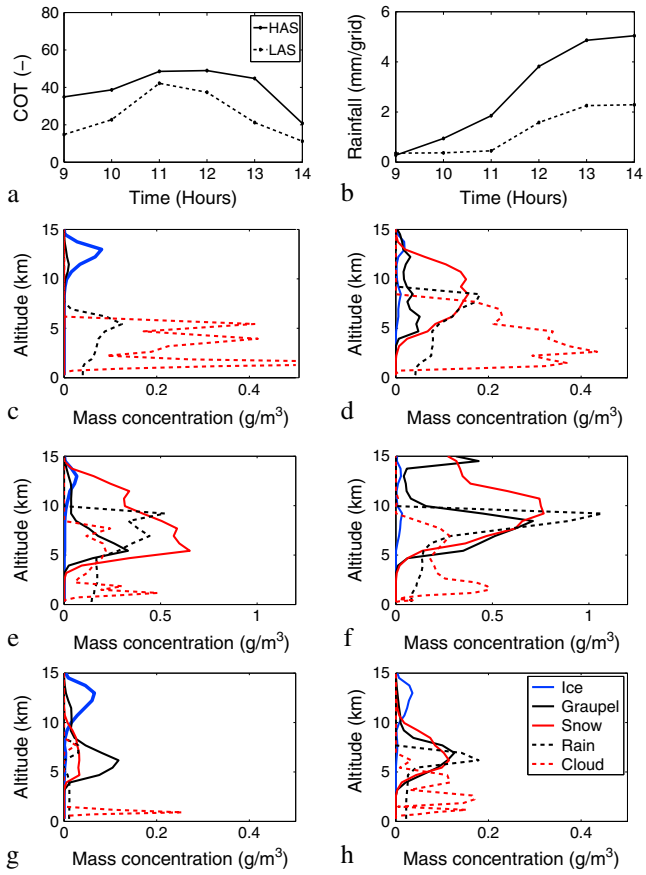

Figure 13. Time series of (a) area averaged COT and (b) rainfall within CAIPEEX region. Vertical distribution of simulated cloud hydrometeor mass concentrations at (c and d) 0900 UTC, (e and f) 1100 h, and (g and h) 1300 h. LAS and HAS run profiles are shown in Figures 13c, 13e, and 13g and Figures 13d, 13f, and 13h, respectively.

higher altitudes over the GB in their analysis of CAIPEEX measurements. The cloud microphysics during Sor23, which had higher CAPE, was mostly dominated by solid-phase hydrometeors (graupel, snow, and ice), while liquid-phase hydrometeors comprised the major portion during Sor25 with lower CAPE.

A comparison of the HAS and LAS results clearly shows that higher aerosol loading is associated with higher COT values as well as the greater accumulation in surface rainfall during both the sorties. There were greater differences during Sor23 compared to Sor25. Comparison of the vertical profiles (Figures 13 and 14) illustrates that the clouds grew vertically upward resulting in higher-cloud top height in the HAS run (b, d, f, and h) as compared to the LAS runs (a, c, e, and g) during all the time slices. A recent satellite based study [*Sengupta et al.*, 2013] also showed that aerosols can potentially result in higher-cloud top height during the Indian monsoon. Moreover, the HAS run simulated greater mass concentration of solid-phase hydrometeors, especially graupel, for both the sorties.

To examine the effect of the higher aerosol concentrations on temperature and updraft velocity, horizontal averages of temperature (T) and vertical wind speed (W) in only cloudy grid points were compared between the LAS and HAS simulations. Differences (HAS-LAS) in mean T and W profiles at lower altitudes below cloud base increased in HAS run as compared to LAS run for both the sorties (Figure 15) due to the increase in concentration of absorbing aerosols. It was also found that the updraft below the freezing level and downdraft above the freezing level were intensified in the HAS run. The magnitude of change in temperature ($\sim 0.4^{\circ}$C) below the cloud layer was more than 2 times higher in case of Sor23 compared to Sor25. As discussed in section 3.2, the mean aerosol loading (and thereby amount of absorbing aerosols) in the GB decreased in phase 2 of monsoon depression compared to phase 1. In addition, the presence of smaller cloud coverage over the averaging box during Sor23 fostered greater interaction between solar radiation and absorbing aerosols, and thus the difference in increase in temperature of air parcels near cloud base during the two

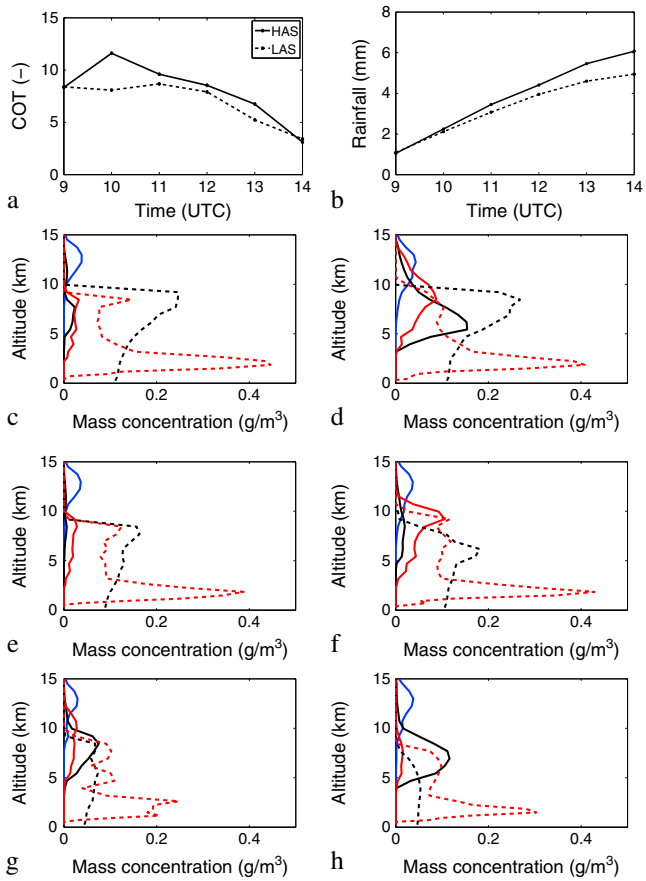

Figure 14. Same as Figure 13 except for the sortie on 25 August 2009.

sorties. The increase in low-level temperature increased the mean CAPE by ~300 J/kg (~50 J/kg) for Sor23 (Sor25). A recent study over Northern India also illustrates that increase in (anthropogenic and natural) dust in elevated aerosol layer increases the radiative heating and can increase the solid-phase hydrometeor concentration [*Dipu et al.*, 2013]. An examination of the tendency terms for the cloud microphysical processes shows a substantial increase in tendencies of droplet condensation, autoconversion of cloud drops to raindrops, water vapor deposition onto graupel, and riming of raindrops to graupel and snow (Figure 15d) in HAS case.

The following chain of feedbacks can explain these aerosol-induced differences. With an increase in anthropogenic aerosol loading in the planetary boundary layer, we found an increase in the mean temperature and convective available potential energy (CAPE). At the same time, the increase in aerosol loading fostered formation of more, smaller cloud droplets near the cloud base. Both these processes resulted in increasing the updraft velocity below the freezing level. Most probably, this increased the upward flux of the cloud droplets across the freezing level. As more cloud droplets now reach above freezing level, the autoconversion rate from cloud droplets to raindrops and thereby the mass concentration of rain increased at higher altitude. This increased upward flux of cloud droplets also leads to an enhancement in the deposition rate and riming of cloud and raindrops into the solid-phase hydrometeors (mainly graupel), as well as shifted the distribution of cloud hydrometeors to higher altitudes. This scenario commonly known as cloud invigoration has been described before [*Andreae et al.*, 2004; *Koren et al.*, 2012; *Li et al.*, 2011] and summarized in *Rosenfeld et al.* [2008]. As a consequence of the increased condensed phase at higher altitudes, the cloud parcels become heavier and the downdraft intensifies above the freezing level. Thus, these aerosol sensitivity experiments illustrate an aerosol-induced cloud invigoration effect during both the sorties, resulting in higher COT and accumulated surface rainfall. In our study, the aerosol-induced increase in CAPE aided the microphysical-dynamical cloud invigoration. The recent study of *Saide et al.* [2015] has also shown that smoke (absorbing aerosols) particles impose both radiative and microphysical impacts on clouds and enhance the severity of thunderstorms and probability of tornado occurrence.

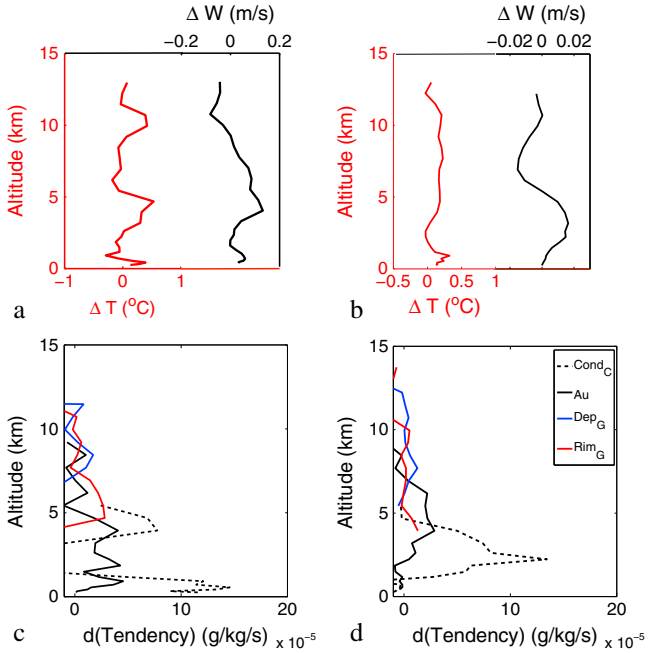

Figure 15. Spatial and temporal mean profiles of difference (HAS-LAS) in temperature (red) as well as vertical wind speed (black) for (a) Sor23 and (b) Sor25. Corresponding mean difference in tendency of droplet condensation ($Cond_C$), autoconversion of droplet to raindrops (Au), deposition of graupel (Dep_G), and rimming of raindrops to graupel/snow(Rim_G) for (c) Sor23 and (d) Sor25, respectively.

5. Summary and Conclusion

This study evaluated the WRF-Chem regional model during a typical monsoon depression period over India between 23 to 29 August 2009 and investigated the aerosol-cloud-rainfall interactions of the associated cloud system over the heavily polluted and densely populated Gangetic Basin (GB).

The study illustrated that WRF-Chem simulated the temporal evolution of meteorological and thermodynamical fields (corresponding to the different phases) fairly well during westward propagation of the monsoon depression across the Indian landmass. Although, the model poorly simulated the magnitude of AOD and aerosol number concentration over the GB using the MACCity+INTEX-B emissions inventory, the spatial distribution of AOD, vertical gradients in moist thermodynamics, and the vertical gradients in cloud properties were well simulated. A comparison of WRF-Chem simulation results over the innermost domain using the MACCity+INTEX-B emissions inventory with a simulation using anthropogenic aerosol emissions increased by a factor of 6 showed that the increase in aerosol emission rates significantly improved the mean magnitude as well as vertical gradients in simulated aerosol, CCN, and cloud microphysical fields. Although the emission inventory and model simulation are for different years, the emissions inventory over the GB may have low-aerosol emissions due to missing contribution from emission sectors (e.g., trash burning and fossil fuel-based cooking stove emissions) and other uncertainties involved in the compilation of emission data.

As the monsoon depression propagated westward from Bay of Bengal (23–24 August) to central India (25–26 August), the aerosol loading over the GB was reduced (as observed from MODIS satellite and simulated by the WRF-Chem model). The inland movement of monsoon depression from phase 1 to phase 2 also brings inflow of cleaner air from BoB as well as the associated cloud systems that ingests the aerosols. These factors along with removal of aerosol by wet scavenging are potential reasons for the reduction in aerosol concentration between these two phases. As the depression propagates to western India (phase 3), rapid aerosol buildup takes place and the aerosol loading over the GB replenishes within 1–2 days.

Two CAIPEEX sorties (23 and 25 August) representing two phases of the westward propagation of the monsoon depression were used to understand the impact of anthropogenic aerosol on cloud microphysics over the GB. The aerosol sensitivity experiments illustrated that higher-aerosol loading fostered perturbations in both cloud dynamics and cloud microphysics leading to invigoration of clouds. The increase in CCN

values near cloud base was associated with an increase in cloud droplet concentrations and a decrease in their effective radius in lower cloud region. Subsequently, the increase in exothermic feedbacks, via higher droplet condensation rates and greater absorption by the higher-aerosol loading, caused an increase in temperature in the lower atmosphere and in CAPE. The change in the thermodynamic environment produced higher vertical wind speeds near cloud base, resulting in uplifting of smaller droplets and eventually causing enhancement in the vertical extent of the cloud and solid-phase hydrometeors mass mixing ratios. Consequently, the cloudiness and accumulated surface rainfall during both the case studies increased in high-aerosol loading scenario compared to the low-aerosol loading scenario during the 5 h analysis time period. Lower anthropogenic aerosol concentrations and CAPE during 25 August sortie was related with lower magnitude in simulated cloud invigoration as compared to 23 August sortie.

This study not only demonstrated the occurrence of cloud invigoration for the first time over the GB but also highlighted the possible influence of absorbing aerosols present below cloud layer on the intensity of cloud invigoration. These case studies (sorties) highlight the importance of microphysical aspect of aerosol impact over the GB, emphasizing the need for future observational and numerical research on aerosol-cloud associations over India. Our conclusion about aerosol-induced cloud invigoration is based on the interpretation that the emission induced difference in aerosol vertical distribution within the boundary layer between LAS and HAS simulation forms the basis of difference in CCN concentration near cloud base (~1 km altitude) and thereby of the differences in cloud dynamics and microphysics. However, other factors affecting CCN concentrations (e.g. variation in vertical velocity, convergence, and dynamical changes due to direct radiative effect of aerosols) and thereby the cloud microphysics were not considered separately in this analysis. These factors along with variations in moist thermodynamic conditions may impact the magnitude of cloud invigoration effect. As such, these conclusions are limited to the case studies investigated here connecting enhanced emissions with cloud perturbations over the GB. Long-term observational and modeling studies are essential to further understand these complex aerosol feedbacks on cloud systems and obtain quantitative relationships between changes in anthropogenic aerosol concentrations and the magnitude of cloud invigoration under different environmental conditions.

Acknowledgments

This project is funded by the Department of Science and Technology, India. National CAIPEEX Program has been funded by Ministry of Earth Sciences (MoES), Government of India, New Delhi, and conducted by IITM. The authors also gratefully acknowledge the financial support given by the Earth System Science Organization, Ministry of Earth Sciences (MoES), and Government of India to conduct this research under Monsoon Mission. Authors are grateful to MoES and IITM for providing the CAIPEEX data for the research purpose in India. The CAIPEEX sorties used in this study can be obtained on request (http://www.tropmet.res.in/caipeex/) from IITM, Pune, India. The in situ surface observational data from IITK are available from the authors upon request (snt@iitk.ac.in). WRF-Chem model is a freely available model (http://www2.mmm.ucar.edu/wrf/users/downloads.html). We are grateful to Rajesh Kumar for his inputs in preparing emission files. The authors would like to thank the National Center for Atmospheric Research (NCAR) Advanced Study Program for the graduate student visitor fellowship and the NCAR Computational and Information Systems Laboratory for the high performance computing support on Yellowstone (ark:/85065/d7wd3xhc). NCAR is sponsored by the U.S. National Science Foundation.

References

Abdul-Razzak, H., and S. J. Ghan (2002), A parameterization of aerosol activation 3. Sectional representation, *J. Geophys. Res.*, *107*, 4026, doi:10.1029/2001JD000483.

Albrecht, B. A. (1989), Aerosols, cloud microphysics, and fractional cloudiness, *Science*, *245*, 1227–1230, doi:10.1126/science.245.4923.1227.

Andreae, M. O., D. Rosenfeld, P. Artaxo, A. A. Costa, G. P. Frank, K. M. Longo, and M. A. F. Silva-Dias (2004), Smoking rain clouds over the Amazon, *Science*, *303*, 1337–1342, doi:10.1126/science.1092779.

Chandrasekar, A., C. Russell Philbrick, B. Doddridge, R. Clark, and P. Georgopoulos (2003), A comparison study of RAMS simulations with aircraft, wind profiler, lidar, tethered balloon and RASS data over Philadelphia during a 1999 summer episode, *Atmos. Environ.*, *37*, 4973–4984, doi:10.1016/j.atmosenv.2003.08.030.

Chapman, E. G., W. I. Gustafson Jr., R. C. Easter, J. C. Barnard, S. J. Ghan, M. S. Pekour, and J. D. Fast (2009), Coupling aerosol-cloud-radiative processes in the WRF-Chem model: Investigating the radiative impact of elevated point sources, *Atmos. Chem. Phys.*, *9*(3), 945–964, doi:10.5194/acp-9-945-2009.

Chen, F., and J. Dudhia (2001), Coupling an advanced land surface-hydrology model with the Penn State-NCAR MM5 modeling system. Part I: Model implementation and sensitivity, *Mon. Weather Rev.*, *129*(4), 569–585.

Colle, B. A., J. B. Wolfe, W. J. Steenburgh, D. E. Kingsmill, J. A. W. Cox, and J. C. Shafer (2005), High-resolution simulations and microphysical validation of an orographic precipitation event over the Wasatch mountains during IPEX IOP3, *Mon. Weather Rev.*, *133*, 2947–2971, doi:10.1175/MWR3017.1.

Cox, R., B. L. Bauer, and T. Smith (1998), A mesoscale model intercomparison, *Bull. Am. Meteorol. Soc.*, *79*, 265–283, doi:10.1175/1520-0477(1998)079<0265:AMMI>2.0.CO;2.

Daggupaty, S. M., and D. R. Sikka (1977), On the vorticity budget and vertical velocity distribution associated with the life cycle of a monsoon depression, *J. Atmos. Sci.*, *34*, 773–792.

Dee, D. P., et al. (2011), The ERA-Interim reanalysis: Configuration and performance of the data assimilation system, *Q. J. R. Meteorol. Soc.*, *137*, 553–597, doi:10.1002/qj.828.

Dey, S., and L. Di Girolamo (2011), A decade of change in aerosol properties over the Indian subcontinent, *Geophys. Res. Lett.*, *38*, L14811, doi:10.1029/2011GL048153.

Dipu, S., T. V. Prabha, G. Pandithurai, J. Dudhia, G. Pfister, K. Rajesh, and B. N. Goswami (2013), Impact of elevated aerosol layer on the cloud macrophysical properties prior to monsoon onset, *Atmos. Environ.*, *70*, 454–467, doi:10.1016/j.atmosenv.2012.12.036.

Eck, T. F., B. N. Holben, J. S. Reid, O. Dubovik, A. Smirnov, N. T. O'Neill, I. Slutsker, and S. Kinne (1999), Wavelength dependence of the optical depth of biomass burning, urban, and desert dust aerosols, *J. Geophys. Res.*, *104*, 31,333–31,350, doi:10.1029/1999JD900923.

Eidhammer, T., M. C. Barth, M. D. Petters, C. Wiedinmyer, and A. J. Prenni (2014), Aerosol microphysical impact on summertime convective precipitation in the Rocky Mountain region, *J. Geophys. Res. Atmos.*, *119*, 11,709–11,728, doi:10.1002/2014JD021883.

Emmons, L. K., et al. (2010), Description and evaluation of the Model for Ozone and Related chemical Tracers, version 4 (MOZART-4), *Geosci. Model Dev.*, *3*, 43–67.

Fan, J., T. Yuan, J. M. Comstock, S. Ghan, A. Khain, L. R. Leung, Z. Li, V. J. Martins, and M. Ovchinnikov (2009), Dominant role by vertical wind shear in regulating aerosol effects on deep convective clouds, *J. Geophys. Res.*, *114*, D22206, doi:10.1029/2009JD012352.

Fast, J., W. I. Gustafson, R. C. Easter, R. A. Zaveri, J. C. Barnard, E. G. Chapman, G. A. Grell, and S. E. Peckham (2006), Evolution of ozone, particulates, and aerosol direct radiative forcing in the vicinity of Houston using a fully coupled meteorology-chemistry-aerosol model, *J. Geophys. Res.*, *111*, D21305, doi:10.1029/2005JD006721.

Ganguly, D., P. Ginoux, V. Ramaswamy, D. M. Winker, B. N. Holben, and S. N. Tripathi (2009), Retrieving the composition and concentration of aerosols over the Indo-Gangetic Basin using CALIOP and AERONET data, *Geophys. Res. Lett.*, *36*, L13806, doi:10.1029/2009GL038315.

Givati, A., and D. Rosenfeld (2004), Quantifying precipitation suppression due to air pollution, *J. Appl. Meteorol.*, *43*, 1038–1056, doi:10.1175/1520-0450(2004)043<1038:QPSDTA>2.0.CO;2.

Gong, S. L., L. A. Barrie, and J.-P. Blanchet (1997a), Modeling sea-salt aerosols in the atmosphere: 1. Model development, *J. Geophys. Res.*, *102*, 3805–3818, doi:10.1029/96JD02953.

Gong, S. L., L. A. Barrie, J. M. Prospero, D. L. Savoie, G. P. Ayers, J.-P. Blanchet, and L. Spacek (1997b), Modeling sea-salt aerosols in the atmosphere: 2. Atmospheric concentrations and fluxes, *J. Geophys. Res.*, *102*, 3819–3830, doi:10.1029/96JD03401.

Granier, C., et al. (2011), Evolution of anthropogenic and biomass burning emissions of air pollutants at global and regional scales during the 1980–2010 period, *Clim. Change*, *109*(1–2), 163–190, doi:10.1007/s10584-011-0154-1.

Grell, G. A., and S. R. Freitas (2014), A scale and aerosol aware stochastic convective parameterization for weather and air quality modeling, *Atmos. Chem. Phys.*, *14*(10), 5233–5250, doi:10.5194/acp-14-5233-2014.

Grell, G. A., S. E. Peckham, R. Schmitz, S. A. McKeen, G. Frost, W. C. Skamarock, and B. Eder (2005), Fully coupled online chemistry within the WRF model, *Atmos. Environ.*, *39*, 6957–6975, doi:10.1016/j.atmosenv.2005.04.027.

Guenther, A., T. Karl, P. Harley, C. Wiedinmyer, P. I. Palmer, and C. Geron (2006), Estimates of global terrestrial isoprene emissions using MEGAN (Model of Emissions of Gases and Aerosols from Nature), *Atmos. Chem. Phys.*, *6*, 3181–3210.

Gustafson, W. I., E. G. Chapman, S. J. Ghan, R. C. Easter, and J. D. Fast (2007), Impact on modeled cloud characteristics due to simplified treatment of uniform cloud condensation nuclei during NEAQS 2004, *Geophys. Res. Lett.*, *34*, L19809, doi:10.1029/2007GL030021.

Hazra, A., V. Mandal, and J.-P. Chen (2013), Study of cloud microphysical properties over India during CAIPEEX using a mesoscale model with new cloud microphysical scheme: Part I, *J. Atmos. Sol. Terr. Phys.*, *93*, 29–44, doi:10.1016/j.jastp.2012.11.010.

Intergovernmental Panel on Climate Change (2007), *Climate Change 2007—The Physical Science Basis: Working Group I Contribution to the Fourth Assessment Report of the IPCC*, Cambridge Univ. Press, Cambridge, U. K., and New York.

Janjic, Z. I. (2002), *Nonsingular Implementation of the Mellor-Yamada Level 2.5 Scheme in the NCEP Meso Model, NCEP Office Note 437*, p. 61.

Khain, A. P., N. Benmoshe, and A. Pokrovsky (2008), Factors determining the impact of aerosols on surface precipitation from clouds: An attempt at classification, *J. Atmos. Sci.*, *65*, 1721–1748, doi:10.1175/2007JAS2515.1.

King, M. D., et al. (2003), Cloud and aerosol properties, precipitable water, and profiles of temperature and water vapor from MODIS, *IEEE Trans. Geosci. Remote Sens.*, *41*, 442–458, doi:10.1109/TGRS.2002.808226.

Konwar, M., R. S. Maheskumar, J. R. Kulkarni, E. Freud, B. N. Goswami, and D. Rosenfeld (2012), Aerosol control on depth of warm rain in convective clouds, *J. Geophys. Res.*, *117*, D13204, doi:10.1029/2012JD017585.

Koren, I., O. Altaratz, L. A. Remer, G. Feingold, J. V. Martins, and R. H. Heiblum (2012), Aerosol-induced intensification of rain from the tropics to the mid-latitudes, *Nat. Geosci.*, *5*, 118–122, doi:10.1038/ngeo1364.

Krishnamurti, T. N., and H. N. Bhalme (1976), Oscillations of a monsoon system. Part I. Observational aspects, *J. Atmos. Sci.*, *33*, 1937–1954.

Kulkarni, J. R., et al. (2012), The Cloud Aerosol Interactions and Precipitation Enhancement Experiment (CAIPEEX): Overview and preliminary results, *Curr. Sci.*, *102*, 413–425.

Kumar, R., M. Naja, G. G. Pfister, M. C. Barth, and G. P. Brasseur (2012a), Simulations over South Asia using the Weather Research and Forecasting model with Chemistry (WRF-Chem): Set-up and meteorological evaluation, *Geosci. Model Dev.*, *5*, 321–343, doi:10.5194/gmd-5-321-2012.

Kumar, R., M. Naja, G. G. Pfister, M. C. Barth, C. Wiedinmyer, and G. P. Brasseur (2012b), Simulations over South Asia using the Weather Research and Forecasting model with Chemistry (WRF-Chem): Chemistry evaluation and initial results, *Geosci. Model Dev.*, *5*, 619–648, doi:10.5194/gmd-5-619-2012.

Kumar, R., M. C. Barth, G. G. Pfister, V. S. Nair, S. D. Ghude, and N. Ojha (2015a), What controls the seasonal cycle of black carbon aerosols in India?, *J. Geophys. Res. Atmos.*, *120*, 7788–7812, doi:10.1002/2015JD023298.

Kumar, R., et al. (2015b), Sources of black carbon aerosols in South Asia and surrounding regions during the Integrated Campaign For Aerosols, Gases And Radiation Budget (ICARB), *Atmos. Chem. Phys.*, *15*(10), 5415–5428, doi:10.5194/acp-15-5415-2015.

Levin, Z., and W. Cotton (2008), *Aerosol Pollution Impact on Precipitation: A Scientific Review*, Springer, Netherlands.

Li, Z., F. Niu, J. Fan, Y. Liu, D. Rosenfeld, and Y. Ding (2011), Long-term impacts of aerosols on the vertical development of clouds and precipitation, *Nat. Geosci.*, *4*, 888–894, doi:10.1038/ngeo1313.

Mayer, S., A. Sandvik, M. O. Jonassen, and J. Reuder (2012), Atmospheric profiling with the UAS SUMO: A new perspective for the evaluation of fine-scale atmospheric models, *Meteorol. Atmos. Phys.*, *116*, 15–26, doi:10.1007/s00703-010-0063-2.

Menon, S., D. Koch, G. Beig, S. Sahu, J. Fasullo, and D. Orlikowski (2010), Black carbon aerosols and the third polar ice cap, *Atmos. Chem. Phys.*, *10*, 4559–4571.

Misenis, C., and Y. Zhang (2010), An examination of sensitivity of WRF/Chem predictions to physical parameterizations, horizontal grid spacing, and nesting options, *Atmos. Res.*, *97*, 315–334, doi:10.1016/j.atmosres.2010.04.005.

Mishra, S. K., and S. N. Tripathi (2008), Modeling optical properties of mineral dust over the Indian Desert, *J. Geophys. Res.*, *113*, D23201, doi:10.1029/2008JD010048.

Mlawer, E. J., S. J. Taubman, P. D. Brown, M. J. Iacono, and S. A. Clough (1997), Radiative transfer for inhomogeneous atmospheres: RRTM, a validated correlated-k model for the longwave, *J. Geophys. Res.*, *102*, 16,663–16,682, doi:10.1029/97JD00237.

Morrison, H., and J. O. Pinto (2005), Mesoscale modeling of springtime arctic mixed-phase stratiform clouds using a new two-moment bulk microphysics scheme, *J. Atmos. Sci.*, *62*, 3683–3704, doi:10.1175/JAS3564.1.

Morrison, H., G. Thompson, and V. Tatarskii (2009), Impact of cloud microphysics on the development of trailing stratiform precipitation in a simulated squall line: Comparison of one- and two-moment schemes, *Mon. Weather Rev.*, *137*, 991–1007, doi:10.1175/2008MWR2556.1.

Nair, V. S., F. Solmon, F. Giorgi, L. Mariotti, S. S. Babu, and K. K. Moorthy (2012), Simulation of South Asian aerosols for regional climate studies, *J. Geophys. Res.*, *117*, D04209, doi:10.1029/2011JD016711.

Potty, K. V. J., U. C. Mohanty, and S. Raman (2000), Numerical simulation of monsoon depressions over India with a high-resolution nested regional model, *Meteorol. Appl.*, *7*, 45–60.

Prabha, T. V., S. Patade, G. Pandithurai, A. Khain, D. Axisa, P. Pradeep-Kumar, R. S. Maheshkumar, J. R. Kulkarni, and B. N. Goswami (2012), Spectral width of premonsoon and monsoon clouds over Indo-Gangetic valley, *J. Geophys. Res.*, *117*, D20205, doi:10.1029/2011JD016837.

Riehl, H. (1971), A weather pattern. (Book reviews: Monsoon meteorology), *Science*, *172*, 691–692, doi:10.1126/science.172.3984.691.

Rosenfeld, D., U. Lohmann, G. B. Raga, C. D. O'Dowd, M. Kulmala, S. Fuzzi, A. Reissell, and M. O. Andreae (2008), Flood or drought: How do aerosols affect precipitation?, *Science*, *321*, 1309–1313, doi:10.1126/science.1160606.

Routray, A., S. Kar, P. Mali, and K. Sowjanya (2014), Simulation of monsoon depressions using WRF-var: Impact of different background error statistics and lateral boundary conditions, *Mon. Weather Rev.*, *142*(10), 3586–3613.

Saide, P. E., et al. (2012), Evaluating WRF-Chem aerosol indirect effects in Southeast Pacific marine stratocumulus during VOCALS-REx, *Atmos. Chem. Phys.*, *12*, 3045–3064, doi:10.5194/acp-12-3045-2012.

Saide, P. E., et al. (2015), Central American biomass burning smoke can increase tornado severity in the U.S., *Geophys. Res. Lett.*, *42*, 956–965, doi:10.1002/2014GL062826.

Seifert, A., C. Köhler, and K. D. Beheng (2012), Aerosol-cloud-precipitation effects over Germany as simulated by a convective-scale numerical weather prediction model, *Atmos. Chem. Phys.*, *12*, 709–725, doi:10.5194/acp-12-709-2012.

Sengupta, K., S. Dey, and M. Sarkar (2013), Structural evolution of monsoon clouds in the Indian CTCZ, *Geophys. Res. Lett.*, *40*, 5295–5299, doi:10.1002/grl.50970.

Shaw, W. J., K. Jerry Allwine, B. G. Fritz, F. C. Rutz, J. P. Rishel, and E. G. Chapman (2008), An evaluation of the wind erosion module in DUSTRAN, *Atmos. Environ.*, *42*, 1907–1921, doi:10.1016/j.atmosenv.2007.11.022.

Shi, J. J., et al. (2010), WRF simulations of the 20–22 January 2007 snow events over Eastern Canada: Comparison with in situ and satellite observations, *J. Appl. Meteorol. Climatol.*, *49*, 2246–2266, doi:10.1175/2010JAMC2282.1.

Sikka, D. R. (1977), Some aspects of the life history, structure and movement of monsoon depressions, *Pure Appl. Geophys.*, *115*, 1501–1529, doi:10.1007/BF00874421.

Skamarock, W. C., J. B. Klemp, J. Dudhia, D. O. Gill, D. M. Barker, M. G. Duda, X.-Y. Huang, W. Wang, and J. G. Powers (2008), A description of the Advanced Research WRF version 3, *NCAR Tech. Note NCAR/TN-475+STR*, Natl. Cent. for Atmos. Res., Boulder, Colo., doi:10.5065/D68S4MVH.

Tao, W.-K., X. Li, A. Khain, T. Matsui, S. Lang, and J. Simpson (2007), Role of atmospheric aerosol concentration on deep convective precipitation: Cloud-resolving model simulations, *J. Geophys. Res.*, *112*, D24S18, doi:10.1029/2007JD008728.

Tao, W.-K., J.-P. Chen, Z. Li, C. Wang, and C. Zhang (2012), Impact of aerosols on convective clouds and precipitation, *Rev. Geophys.*, *50*, RG2001, doi:10.1029/2011RG000369.

Teller, A., and Z. Levin (2006), The effects of aerosols on precipitation and dimensions of subtropical clouds: A sensitivity study using a numerical cloud model, *Atmos. Chem. Phys.*, *6*, 67–80.

Twomey, S. (1977), The influence of pollution on the shortwave albedo of clouds, *J. Atmos. Sci.*, *34*, 1149–1154.

van den Heever, S. C., G. G. Carrió, W. R. Cotton, P. J. Demott, and A. J. Prenni (2006), Impacts of nucleating aerosol on Florida storms. Part I: Mesoscale simulations, *J. Atmos. Sci.*, *63*, 1752–1775, doi:10.1175/JAS3713.1.

Venkata Ratnam, J., and E. A. Cox (2006), Simulation of monsoon depressions using MM5: Sensitivity to cumulus parameterization schemes, *Meteorol. Atmos. Phys.*, *93*(1–2), 53–78, doi:10.1007/s00703-005-0160-9.

Wang, H., W. C. Skamarock, and G. Feingold (2009), Evaluation of scalar advection schemes in the advanced research WRF model using large-eddy simulations of aerosol-cloud interactions, *Mon. Weather Rev.*, *137*, 2547–2558, doi:10.1175/2009MWR2820.1.

Wang, Y., J. Fan, R. Zhang, L. R. Leung, and C. Franklin (2013), Improving bulk microphysics parameterizations in simulations of aerosol effects, *J. Geophys. Res. Atmos.*, *118*, 5361–5379, doi:10.1002/jgrd.50432.

Wiedinmyer, C., S. K. Akagi, R. J. Yokelson, L. K. Emmons, J. A. Al-Saadi, J. J. Orlando, and A. J. Soja (2011), The Fire INventory from NCAR (FINN): A high resolution global model to estimate the emissions from open burning, *Geosci. Model Dev.*, *4*, 625–641, doi:10.5194/gmd-4-625-2011.

Wiedinmyer, C., R. J. Yokelson, and B. K. Gullett (2014), Global emissions of trace gases, particulate matter, and hazardous air pollutants from open burning of domestic waste, *Environ. Sci. Technol.*, *48*, 9523–9530, doi:10.1021/es502250z.

Yang, Q., et al. (2011), Assessing regional scale predictions of aerosols, marine stratocumulus, and their interactions during VOCALS-REx using WRF-Chem, *Atmos. Chem. Phys.*, *11*(23), 11,951–11,975, doi:10.5194/acp-11-11951-2011.

Yoon, J.-H., and T.-C. Chen (2005), Water vapor budget of the Indian monsoon depression, *Tellus A*, *57*(5), 770–782, doi:10.1111/j.1600-0870.2005.00145.x.

Zaveri, R. A., and L. K. Peters (1999), A new lumped structure photochemical mechanism for large-scale applications, *J. Geophys. Res.*, *104*, 30,387–30,415, doi:10.1029/1999JD900876.

Zaveri, R. A., R. C. Easter, J. D. Fast, and L. K. Peters (2008), Model for Simulating Aerosol Interactions and Chemistry (MOSAIC), *J. Geophys. Res.*, *113*, D13204, doi:10.1029/2007JD008782.

Zhang, J., W. Gong, W. R. Leaitch, and J. W. Strapp (2007), Evaluation of modeled cloud properties against aircraft observations for air quality applications, *J. Geophys. Res.*, *112*, D10S16, doi:10.1029/2006JD007596.

Zhang, Q., et al. (2009), Asian emissions in 2006 for the NASA INTEX-B mission, *Atmos. Chem. Phys.*, *9*, 5131–5153.